A finite strain contact model for mixed lubricated surfaces in forming processes

Mariela Luege [a,*], Antonio Orlando [b], Johann Sienz [c]

[a] CONICET, Instituto de Estructuras, Universidad Nacional de Tucumán, Av. Independencia 1800, 4000 San Miguel de Tucumán, Tucumán, Argentina
[b] Instituto de Estructuras & Departamento de Mecánica, Universidad Nacional de Tucumán, Av. Independencia 1800, 4000 San Miguel de Tucumán, Tucumán, Argentina
[c] College of Engineering, Swansea University, Singleton Park, Swansea SA2 8PP, UK

ARTICLE INFO

ABSTRACT

For an accurate simulation of forming processes, it is of paramount importance to model the different lubrication regimes that can develop at the contact interface. These might vary from zone to zone of the forming piece, and from one regime to another, resulting in forces of different nature and magnitude. In these cases, the use of the classical Coulomb friction law will be clearly not sufficient to capture, in a suitable manner, the variety of forces applied on the forming piece.

Objective of this paper is the development of a constitutive model for the contact interface that is able to capture the different lubrication regimes. The load bearing capacity of the contact interface is assumed to be the resultant of two mechanisms: dry friction arising from the solid contact asperities, and hydrodynamic fluid film lubrication. The activation of one, the other or both mechanisms is controlled by a parameter α that, in the proposed model, depends on the current value of the sliding velocity V, the interfacial separation D and the surface roughness σ_s. The functional relation defining α can be derived either from experimental fitting of some parameters, which can be introduced into a predefined analytical expression designed to reflect the variation of the different regimes, or from the application of a sequential multiscale analysis through the use of microscale models.

The model is formulated with respect to a convected reference frame, so to make it amenable for large deformation simulations. The numerical integration scheme of the resulting initial constitutive value problem is presented and implemented into an explicit finite element code. The mechanisms of the interface model have been separately tested and the numerical results correlate well with the available experimental findings. Comparisons with the Coulomb friction model are also provided. The applicability of the model for forming simulations is then demonstrated by reproducing the manufacturing of a ridge on an aluminum tube for the cosmetic industry, using the hydroforming technique. Both an elastomer and the fluid have been employed as pressure medium, and their performance has been compared in terms of the stresses and deformations produced in the finished product.

© 2013 Elsevier Inc. All rights reserved.

1. Introduction

In forming processes, the consideration of the tribological conditions at the interface between the die and the work piece represents a fundamental concern of the whole process design. Given the high contact pressures and the large contact surfaces, very high friction forces are generated that might limit the relative movement between the workpiece and the die. This

* Corresponding author.
E-mail address: mluege@herrera.unt.edu.ar (M. Luege).
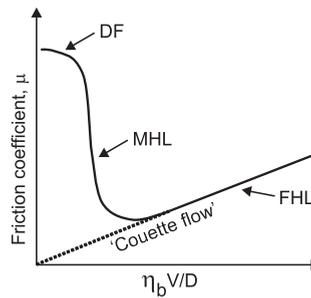
Fig. 1. Schematic representation of a traditional Stribeck curve, with indication of the lubrication regimes: DF (dry friction), MHL (Mixed Hydrodynamic Lubrication), FHL (Full Hydrodynamic Lubrication).
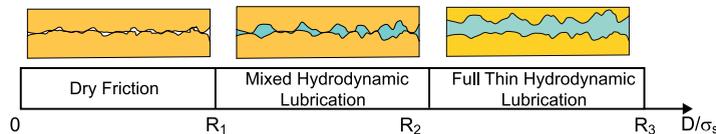
Fig. 2. Schematic representation of the different lubrication regimes in function of the ratio D/σ_s. The quantities R_1, R_2 and R_3 are characteristic values dependent on the tribological system, marking the transition from one regime to another [3].In this picture, the surface roughness is shown amplified for purpose of illustration.

can lead to thinning of the expansion zone, failure bursting, and can jeopardise the surface integrity of the work piece, just to mention few of the problems that might occur. The application of lubricants, as means to reduce the above effects, requires the consideration of the different regimes that are expected to occur along the different forming zones, depending on the sliding velocity, pressure and contact surface conditions, surface roughness, and interfacial separation between the surfaces. A pictorial representation of the friction behaviour of confined fluid thin lubricants is traditionally provided by the Stribeck curve, depicted in Fig. 1, which shows the friction coefficient μ as a function of the bulk fluid viscosity η_b, the sliding speed V and the film thickness D [1]. Even though this representation is not universally accepted as fully representative of the friction variation, with some researchers suggesting an improved Stribeck curve based on parameters easily accessible under engineering conditions [2], what matter to note for the interface behaviour, is however the existence of three zones associated with different load bearing mechanisms of the contact interface. The three zones are referred to as boundary lubrication or dry-friction regime, mixed or partial lubrication regime and full thin lubrication regime.

Fig. 2 illustrates the different regimes, which are identified by characteristic values of the ratio of the interfacial separation D to the surface roughness, characterized by the standard deviation σ_s of the assumed Gaussian distribution of the asperity heights.

For relatively thick lubricated surfaces the resistance to motion is determined by the lubricant bulk viscosity η_b. In presence of high pressure load and low sliding velocity, the surface asperities penetrate the lubrication layer, are separated by each other only by films of molecular thickness, and lubrication is said to be under boundary conditions or dry friction. The lubrication regime between these two is referred to as mixed lubrication regime and in this case, the tangential force applied to the surface depends on both the solid contact asperities and the interstitial lubricant.

The knowledge of the friction map for the tribological system that one is examining permits the assessment of different type of actions applied on the moving surfaces. The Stribeck curve, or likewise any boundary friction map that reflects accurately the energy dissipation in the interface [2], provides therefore a constitutive formulation for the forces transmitted through the contact interface. Their use, in place of Coulomb friction with viscous regularization for lubricated contacts, has been since advocated for the numerical simulations of those processes where there is need to account judiciously for the different tribological conditions that can arise [4,2].

In spite of the several experimental and theoretical studies that have been performed to date to elucidate and to model the different mechanisms responsible of each of the above regimes, the actual use of such friction maps for numerical simulations of forming processes appears not yet having been fully explored. While it is unanimously recognized, especially for lubricants not having a fast relaxation process, the need of improving the modelling of the contact interface, the current body of works on this subject focuses on only one or the other feature of the complex friction mechanism. Finite element simulations of sheet metal forming processes carried out in [5], for instance, employ a model of dry friction where only the ploughing and adhesion mechanisms of the boundary layer are taken into account (see also [6] for another model accounting for these mechanisms), whereas the authors in [7] explore, mainly from the computational point of view, the use of rate-and-state dependent friction laws to model dry-friction in the context of large deformation problems. A mixed lubrication model for deep drawing processes, which accounts for the contact area evolution based on some available asperity flattening mechanisms has been developed in [8], whereas [9] presents finite element simulations of sheet metal forming processes using the mixed hydrodynamic lubrication model proposed in [10], which combines the Greenwood Williamson model for the normal contact pressure [11] and the film thickness solution of the hydrodynamic lubrication model of Moes [12,13] for fully flooded smooth rigid line contacts.

The above studies provide valuable insight in the physics and modelling of the different friction mechanisms. Nevertheless, they appear limited in the scope for real applications, and are generally computationally demanding. Aim of this work is to propose a simple model, in the framework of large deformations following [14,7], which goes beyond the Coulomb friction law, in the sense that it accounts for the different lubrication regimes as described above, and can be easily used for the preliminary design of large scale applications.

The model proposed in this work adopts the load sharing assumption introduced in [15,16] which consists of taking the action applied on the lubricated contact surfaces as a convex combination of the load bearing contributions deriving from the dry friction and the full hydrodynamic lubrication mechanisms. The contribution of each of the two mechanisms is captured through a variable α that depends on the interfacial separation D, the sliding velocity V and surface roughness. The functional relation that gives α could be defined either from experiments or, as application of a sequential multiscale analysis, α could be computed using microscale models for the interface. In this manner, the proposed model retains the simplicity of a phenomenological approach and, meanwhile, it includes more refined information with a fraction of cost of lower computational demand, compared to a genuinely on-fly multiscale analysis. The latter would indeed require a multiscale analysis at each point of the slave element which is projection of the master node, making prohibitive the simulation of large scale computations for real applications, such as in forming processes.

After this brief introduction, the following Section 2 describes the constitutive model for the contact interface, illustrating and discussing the constitutive assumptions for each of the contributing mechanisms. The load sharing assumption is introduced to describe the friction conditions in the mixed lubrication regime, with the definition of the constitutive parameter α. Section 3 presents the adopted scheme for the numerical integration of the constitutive equations, in view of its implementation into the explicit FE code STAMPACK®, particularly suitable for metalforming processes simulations [17,18]. The selection of an explicit FE code was dictated by the observation that, for such type of simulations, explicit codes represent still the first choice in industrial applications. This is because of their lower computational cost, which scales almost linearly with the problem size, and of the relative ease for the implementation of the contact constraints in large deformations [19]. A real industrial application for the design of a ridge on an aluminum tube for the cosmetic industry is then carried out and discussed in Section 4. This study is preceded by two numerical examples where the single components of the contact interface are tested and validated against experimental results. In the final Section 5, conclusions on this work are drawn.

2. Constitutive model for dry, mixed and fully lubricated contact

This section describes the constitutive model for the contact interface by defining one constitutive equation for the normal contact pressure t_N and one for the tangential traction $\boldsymbol{t}_T(\boldsymbol{X}, t)$. These constitutive equations relate t_N and $\boldsymbol{t}_T(\boldsymbol{X}, t)$ to their respective kinematic dual variables and to possible internal variables. For their formulation, the contributing contact mechanisms, either derived from dry friction, or from the hydrodynamic action of the lubricant or from both, are taken into account. The constitutive equations are formulated in a reference frame convected with the deformation of the bodies in contact. Also, in the following, it will be assumed that the evaluation of the normal contact pressure is decoupled from the evaluation of the tangential traction, and that the system is sufficiently large to be self–averaging. The latter assumption means that an effective dependence of the static variables on the macroscopic primary variables, such as time, irreversible sliding distance and sliding velocity, can be postulated.

2.1. Contact kinematics

The kinematic relations describing the two-body large deformation contact problem are formulated by assuming that the boundaries of the two bodies are smooth and by using a convected reference frame as described in [20,14,21]. Standard notation given in [20,14] is thus followed. This is next succinctly summarized with the purpose of introducing the relevant notation, see also Fig. 3. Let $\mathcal{B}^1$ and $\mathcal{B}^2$ denote the two bodies that come into contact, and denote by $\boldsymbol{x} = \boldsymbol{\varphi}_t^1(\boldsymbol{X})$ and $\boldsymbol{y} = \boldsymbol{\varphi}_t^2(\boldsymbol{Y})$ the corresponding deformation mappings at time $t \in I$, with $I = [0, T]$ the time interval of interest. The boundary Γ^i of each body, for $i = 1, 2$, can be partitioned in three parts: $\Gamma_u^i, \Gamma_\sigma^i$ and Γ_c^i. The parts Γ_u^i and Γ_σ^i have prescribed displacements and tractions, respectively, whereas Γ_c^i, is the part of the boundary that is expected to come into contact with the other body at a certain instant $t \in I$. On Γ_c both the contact and friction conditions must be formulated [22].

For any $\boldsymbol{X} \in \mathcal{B}^1$, the physical requirement of impenetrability and compression interaction between the two bodies will be expressed in terms of the gap function $g(\boldsymbol{X}, t)$ i.e. the distance of $\boldsymbol{x} \in \boldsymbol{\varphi}_t^1(\Gamma_c^1)$ to $\boldsymbol{\varphi}_t^2(\Gamma_c^2)$ defined as

$$g(\boldsymbol{X}, t) = -\boldsymbol{v} \cdot \left[\boldsymbol{\varphi}_t^1(\boldsymbol{X}) - \boldsymbol{\varphi}_t^2(\bar{\boldsymbol{Y}}) \right], \tag{2.1}$$

where $\bar{\boldsymbol{Y}}$ is the point of the initial configuration whose image by $\boldsymbol{\varphi}_t^2$ is $\bar{\boldsymbol{y}}$, with $\bar{\boldsymbol{y}} = \boldsymbol{\varphi}_t^2(\bar{\boldsymbol{Y}})$ being the closest point of $\boldsymbol{\varphi}_t^2(\Gamma_c^2)$ to $\boldsymbol{x} = \boldsymbol{\varphi}_t^1(\boldsymbol{X})$ and $\boldsymbol{v}$ the outward normal to the surface $\boldsymbol{\varphi}_t^2(\Gamma_c^2)$ at $\bar{\boldsymbol{y}}$. A basis $\boldsymbol{\tau}_\alpha$ can then be constructed at each contact point $\bar{\boldsymbol{y}}$ by evaluating the partial derivatives of the deformation field $\boldsymbol{\varphi}_t^2$ with respect to the convective coordinates ξ^α, at the coordinates $\bar{\xi}^\alpha$ of the point $\bar{\boldsymbol{Y}}(\boldsymbol{X}, t)$.

The relative displacement between the two bodies in contact is then given by

$$\boldsymbol{g}_T(\boldsymbol{X}) = \int_{t_s}^t \dot{\bar{\xi}}^\alpha \boldsymbol{\tau}_\alpha d\tau, \tag{2.2}$$
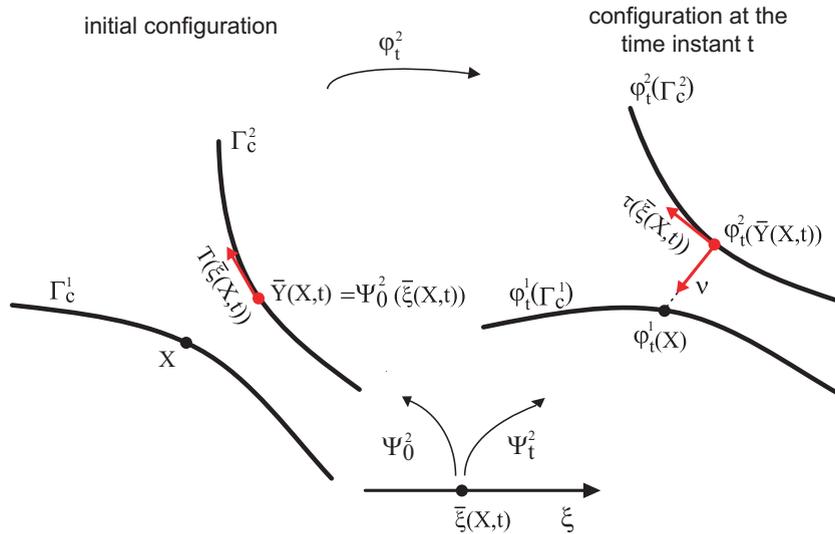
Fig. 3. Basic notation for the kinematics of the two-body large deformation problem with parametrization of the contact surfaces in terms of the local convective coordinates. In this formulation, a basis $t_\alpha = \Psi^2_{0,\alpha}$ of the tangent manifold associated with each point X of the initial configuration and parametrized by $\xi(X,t)$ is defined. The basis t_α is then convected with the point as it moves and gives $\tau_\alpha = \Psi^2_{t,\alpha}$, vector basis of the tangent manifold of the current configuration. The symbol Ψ^2_t denotes the parametric representation of the manifold $\varphi^2_t(\Gamma^2_c)$ at the time instant t [20,23,21], whereas $\Psi^2_{t,\alpha}$ represents the partial derivative of Ψ^2_t with respect to the curvilinear coordinate ξ_α.

where t_s is the time instant when the two surfaces come into contact, t is the current time instant, and $\dot{\bar{\xi}}^\alpha$ is the time derivative of the curvilinear coordinate ξ^α evaluated at $\bar{Y}(X,t)$. The tangential relative velocity is computed as the Lie derivative of the tangential slip distance g_T with respect to the surface velocity $v = v^2$ with $v^2 = \frac{d}{dt}\varphi^2_t(\bar{Y}(X,t))$. This derivative is shown to be equal to the time derivative of g_T in the convective current base τ_α [14], i.e.

$$\mathcal{L}_v g_T = \dot{\bar{\xi}}^\alpha \tau_\alpha. \tag{2.3}$$

Remark 2.1. In the case of rough contact surfaces, the kinematic contact relations defined above can still be used, with the meaning that now such quantities refer to the mean surfaces of the asperity heights distribution, with such mean surfaces assumed to be smooth. The surface roughness can then be taken into account through the following relation

$$D = g - h_1 - h_2, \tag{2.4}$$

where D is the current interfacial separation (or film thickness), and h_1 and h_2 define the roughness profile of surface 1 and surface 2 with respect to the mean surfaces of their respective asperity heights distributions, with $h_i > 0$ if corresponding to elevation. Fig. 4 displays the definition and the relation between these quantities [3,24]. □

2.2. Load sharing assumption

The formulation of the constitutive model for the contact interface in terms of $\mathcal{L}_v g_T$ requires the definition of the dual variable of $\mathcal{L}_v g_T$ which is the tangential traction $t_T(X,t)$. Noting that $\mathcal{L}_v g_T$ is a vector resolved in terms of the spatial bases τ_α, it is shown in [14] that $t_T(X,t)$ is obtained by resolving the Piola nominal contact traction $T(X,t)$ at $X \in \Gamma^1_c$, in terms of the spatial bases τ_α, that is,

$$T(X,t) = -t_N(X,t)v + t_T(X,t), \tag{2.5}$$
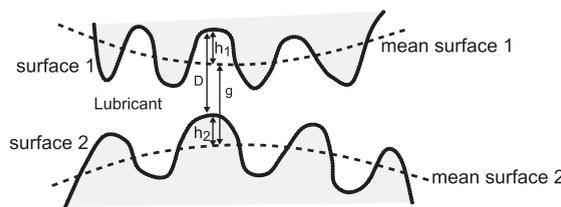
Fig. 4. Sketch of the surface roughness with indication of the geometrical gap g, heights h_i of the asperities evaluated with respect to their respective mean surfaces, and interfacial distance D (film thickness), with $h_i > 0$ if it relates to elevation.

where $\boldsymbol{v}$ is the outward normal to $\boldsymbol{\varphi}_t^2(\Gamma_c^2)$ at $\bar{\boldsymbol{y}}$ (normal to the spatial bases $\boldsymbol{\tau}_\alpha$), t_N is the nominal contact pressure (positive if compressive), and $\boldsymbol{t}_T$ is the spatial frictional traction. Since the frictional traction $\boldsymbol{t}_T$ lies in the tangent space of $\boldsymbol{\varphi}_t^2(\Gamma_c^2)$ at $\bar{\boldsymbol{y}}$, it can be expressed in the convective current base $\boldsymbol{\tau}_\alpha$ as follows

$$\boldsymbol{t}_T(\boldsymbol{X}, t) = t_{t_\alpha}(\boldsymbol{X}, t)\boldsymbol{\tau}^\alpha, \tag{2.6}$$

where $\boldsymbol{\tau}^\alpha = m^{\alpha\beta}\boldsymbol{\tau}_\beta$ represents the dual basis to $\boldsymbol{\tau}_\beta$. The coefficients $m^{\alpha\beta} = \boldsymbol{\tau}^\alpha \cdot \boldsymbol{\tau}^\beta$ and $m_{\alpha\beta} = \boldsymbol{\tau}_\alpha \cdot \boldsymbol{\tau}_\beta$ are referred to as metric coefficients and characterize metric properties of the deformed configuration. Because of (2.6), a contact law relating the tangential part of $\boldsymbol{T}$ to the tangential relative velocity (2.3) will therefore provide a spatial formulation of the frictional contact (for further details, refer to [20] and [14, pag 120]).

The constitutive model for the interface is therefore obtained by formulating one constitutive equation for t_N and one for $\boldsymbol{t}_T$. Given that under mixed lubricated conditions the mechanisms that contribute to the contact interface bearing derive from the hydrodynamic force of the lubricant and from the contact force at the solid asperities, an additive load sharing assumption, as proposed by [15,16], is made for both the evaluation of the total nominal contact pressure, and the total nominal tangential traction. This means that the total nominal pressure is assumed to be given as

$$t_N = t_{N,DF}^{nom} + t_{N,HL}^{nom} \tag{2.7}$$

and an alike relation holds for the total nominal tangential traction which is stated in the form

$$\boldsymbol{t}_T = (1 - \alpha)\boldsymbol{t}_{T,DF} + \alpha\boldsymbol{t}_{HL}, \tag{2.8}$$

(refer to [25, Eq. (15) and Eq. (32)] where analogous relations are also given). In Eq. (2.7), $t_{N,DF}^{nom}$ is the nominal normal pressure resulting from the contact of the solid asperities, whereas $t_{N,HL}^{nom}$ is the nominal normal lubricant pressure. This relation holds for all the lubrication regimes, given that $t_{N,HL}^{nom} = 0$ when only the dry friction is active, and $t_{N,DF}^{nom} = 0$ when only the hydrodynamic lubrication regime is active. For the mixed hydrodynamic regime, both the actions will be present. Eq. (2.7) has been written in terms of the nominal pressure, i.e. of the pressure referred to the unit nominal area. In this manner, it is possible to quantify the relative importance of the two mechanisms through the definition of the coefficient $\alpha \in [0, 1]$ (whose reciprocal is called scaling factor in [15,16]), given as the ratio of $t_{N,DF}^{nom}$ to t_N, i.e. $\alpha = t_{N,DF}^{nom}/t_N$. The coefficient α depends on the relative sliding velocity $|\mathcal{L}_v\boldsymbol{g}_T|$ and on the interfacial separation D. For its evaluation, see discussion below in Section 2.5. Once α is known, one can then evaluate the total nominal tangential traction through Eq. (2.8) where $\boldsymbol{t}_{T,DF}$ is the tangential friction at the solid asperities and $\boldsymbol{t}_{T,HL}$ is the tangential stress applied by the lubricant.

Following the above assumptions, the constitutive equation for the contact interface is therefore obtained by giving constitutive relations for $t_{N,DF}^{nom}, t_{N,HL}^{nom}, \boldsymbol{t}_{T,DF}$ and $\boldsymbol{t}_{T,HL}$.

Remark 2.2. The concept of load sharing is relatively straightforward; the two bearing mechanisms are assumed to act in parallel and, in its simplest form, are considered to be one independent to the other. A detailed analysis should include an interaction between the two mechanisms, of the type fluid–solid interaction, especially when surface deformations play a relevant influence on the fluid pressure. The concept, as here used, is, nevertheless, quite consolidated in the literature as first approximation, and represents the underlying assumption in many studies on mixed hydrodynamics lubrication [26,25,27,28]. □

2.3. Normal pressure: Evaluation of $t_{N,DF}^{nom}$

Within the proposed framework, different constitutive equations can be used for $t_{N,DF}^{nom}$, according, for instance, to the geometrical type of contact (point or line contact), and the type of contact surfaces (rough hard surface on smooth hard surface; rough soft surface on smooth hard surface; rough hard surface on rough hard surface; rough hard surface on rough soft surface; rough soft surface on rough soft surface; smooth soft surface on smooth soft surface). One is mainly looking for an expression that relates $t_{N,DF}^{nom}$ to D which is generally obtained by applying the relevant contact mechanics theory (see for instance [29,11,30–32]) or by experiment [33–35]. For the modelling of the mixed lubrication regime, the constitutive equation for $t_{N,DF}^{nom} = t_{N,DF}^{nom}(D)$ can range from its simplest form, with a linear dependence on D of the type given by Eq. (2.12) below, for instance, to a more elaborated one such as the one given in [30] or in [11], where different mechanical aspects of the contact are taken into account. Next, for illustrative purpose, the Greenwood and Williamson model introduced in [11] is recalled. According to this model, the nominal normal pressure at the asperities, referred to the nominal area, is given by

$$t_{N,DF}^{nom,WG} = \frac{2}{3}n\beta\sigma_s\sqrt{\frac{\sigma_s}{\beta}}E'\frac{1}{\sqrt{2\pi}}\int_{D/\sigma_s}^\infty \left(s - \frac{D}{\sigma_s}\right)^{3/2}\exp\left(-\frac{s^2}{2}\right)ds, \tag{2.9}$$

where the effective modulus E' is such that $1/E' = (1 - v_1^2)/E_1 + (1 - v_2^2)/E_2$, with E_1 and E_2 the Young modulus, and v_1 and v_2 the Poisson's ratios, of the two surfaces in contact, whereas n, β and σ_s are parameters characterizing the surface roughness. In particular, $n\,[m^{-2}]$ represents the asperities density, $\beta\,[m]$ the average radii of the asperities and $\sigma_s\,[m]$ the standard
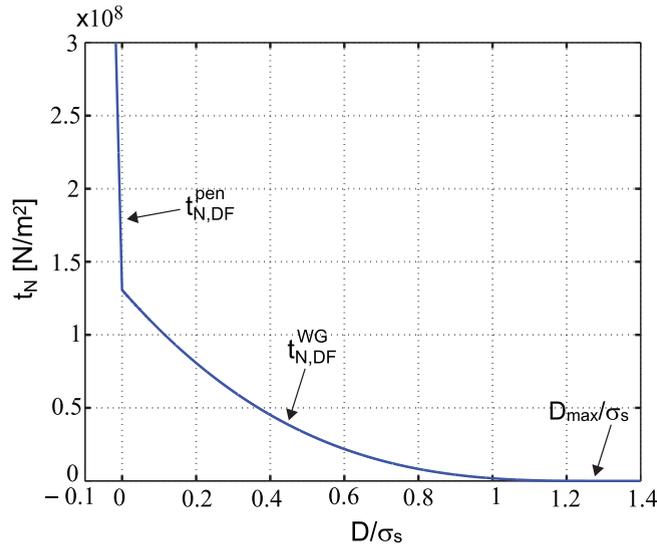
Fig. 5. Variation of $t_{N,DF}^{nom}$ as given by Eq. (2.13) using the Greenwood and Williamson contact model and the penalty given by Eq. (2.12).

deviation of the heights distribution of the summits, assumed of Gaussian type [11]. The upper integration limit in (2.9) is replaced with the finite adimensional value $R_3 = D_{max}/\sigma_s$ that marks the transition from the mixed lubrication to the full hydrodynamic lubrication[1], hence

$$t_{N,DF}^{nom,WG} = \begin{cases} \frac{2}{3}n\beta\sigma_s\sqrt{\frac{\sigma_s}{\beta}}E'\frac{1}{\sqrt{2\pi}}\int_{D/\sigma_s}^{R_3}\left(s - \frac{D}{\sigma_s}\right)^{3/2}\exp\left(-\frac{s^2}{2}\right)ds & \text{for } 0 \leqslant \frac{D}{\sigma_s} \leqslant R_3, \\ 0 & \text{for } \frac{D}{\sigma_s} > R_3. \end{cases} \tag{2.10}$$

As given by Eq. (2.10), $t_{N,DF}^{nom,WG}$ is defined also for negative values of *D*. To avoid such values for *D*, which would violate the impenetrability constraint, a penalty method is employed, which is here enforced through the constitutive equation [34]. This can be done as an exterior penalty method, which is the manner that is commonly used in practice, or as barrier method [34]. An instance of enforcement through the barrier method is given by considering the following function

$$t_{N,DF}^{nom,pen} = \left\langle -\epsilon\log\left(\frac{D}{\sigma_s R_1}\right)\right\rangle_+^2, \tag{2.11}$$

with $R_1 = D_{min}/\sigma_s$ and $\langle a\rangle_+ := max\{a, 0\}$, whereas with an exterior penalty, where small negative values of *D* would be in this case allowed, one assumes

$$t_{N,DF}^{nom,pen} = K_N\left\langle -\frac{D}{\sigma_s}\right\rangle_+, \tag{2.12}$$

with ϵ and K_N being the respective penalty factors. The regularized nominal normal contact pressure is then defined as

$$t_{N,DF}^{nom} = t_{N,DF}^{nom,WG} + t_{N,DF}^{nom,pen}. \tag{2.13}$$

Fig. 5 displays $t_{N,DF}^{nom}$, as given by Eq. (2.13), using (2.10) with: $D_{max} = 250 \cdot 10^{-9}\,m, n = 2.5 \cdot 10^{10}\,m^{-2}, \beta = 10 \cdot 10^{-6}\,m$, $\sigma_s = 0.2 \cdot 10^{-6}\,m$ and $E' = 1.50 \cdot 10^{11}\,N/m^2$ taken from [26], and (2.12) with $K_N = 1 \cdot 10^{10}\,N/m^2$.

2.4. Normal pressure: evaluation of $t_{N,HL}^{nom}$

The lubricant hydrodynamic normal pressure $t_{N,HL}^{nom}$ should be obtained by the solution of the Reynolds equation which represents a dimensional reduction of the Navier–Stokes equations for thin film viscous flow. The Reynolds equation is, in general, a free boundary problem for the possible occurrence of cavitation, which is coupled to the deformation of the surfaces, in the case of elastohydrodynamic lubrication. Several solution methods have been advanced in the literature. The analytical solutions, currently available, have been obtained for particular geometry and mainly for full film hydrodynamic conditions, by neglecting the solid surfaces deformation, [1,36], whereas the numerical methods [37,38,3,39] and the approximate solutions [12,10] contemplate more general cases and apply to elastohydrodynamic, as well, where also the

---

[1] D_{max}, defined in the following, is the value of the film thickness such that the FHL is realized for any value of the sliding velocity *V*.

deformation of the surfaces is taken into account. In this paper, an approximate solution is considered, which represents for some aspects a further simplification of the one proposed by [12,10]. By assuming that cavitation does not occur and that enough lubricant is supplied to the contact (condition known as fully flooded lubrication as opposite to starved lubrication), an approximation for the fluid pressure in the full hydrodynamic regime is proposed in the form

$$t_{N,HL}^{nom} = \delta\eta_b \frac{|\mathcal{L}_v g_T|}{D}. \tag{2.14}$$

In (2.14), the parameter δ depends on the geometry of the tribological system whereas the bulk viscosity η_b is assumed in this paper to be constant with respect to the pressure and temperature. This approximation appears quite reasonable. The analytical solutions of the Reynolds equation for the simplified geometry reported in [1] show indeed for $t_{N,HL}^{nom}$ a functional dependence on the sliding velocity $|\mathcal{L}_v g_T|$ and on the interfacial separation D of the type given in (2.14). Furthermore, relations of the type (2.14) have also been contemplated in [40,41] concerning with the well posedeness of the lubricated contact problem.

Remark 2.3. Notice that due to the assumption of no-cavitation, one will need to check that the computed normal fluid pressure does not drop below the so-called cavitation pressure. □

2.5. Normal pressure: Coefficient α and evaluation of t_N

The coefficient $\alpha \in [0, 1]$, defined in Section 2.2, weights the lubricant and the solid asperities contact mechanisms to the global loading bearing capacity of the contact interface. By definition, α characterizes the mixed hydrodynamic regime and is introduced as a constitutive relation which must be evaluated for the tribological system that one is examining once the corresponding Stribeck curve is known. The Stribeck curve can be obtained either from the experiments [26], or from computation by using multiscale models as in [26,10,25]. For the purpose of demonstrating the viability of this approach based on the use of the parameter α, a relatively simple analytical expression for α, from [42], is next taken into account,

$$\alpha = \begin{cases} \min\left(\frac{\langle D-D_{min}\rangle_+}{D_{max}-D_{min}}, 1\right) & \text{if } |\mathcal{L}_v g_T| < \zeta \frac{\langle D_{max}-D\rangle_+}{\langle D-D_{min}\rangle_+}, \\ 1 & \text{if } |\mathcal{L}_v g_T| \geqslant \zeta \frac{\langle D_{max}-D\rangle_+}{\langle D-D_{min}\rangle_+}, \end{cases} \tag{2.15}$$

with D_{max} and D_{min} the maximum and minimum film thickness for which one has the pure viscous and the pure frictional regime, respectively, for any value of the sliding velocity, whereas ζ is a parameter that must be determined by fitting experimental results. The evaluation of ζ is discussed in the next Section. The term

$$V_{cr}(D) := \zeta \frac{\langle D_{max}-D\rangle_+}{\langle D-D_{min}\rangle_+}, \tag{2.16}$$

displayed in Fig. 6 for convenience, denotes, by its same definition, a critical velocity which marks the transition from the mixed regime to the pure viscous one. In agreement with the general experimental evidence described in Section 1, Eq.
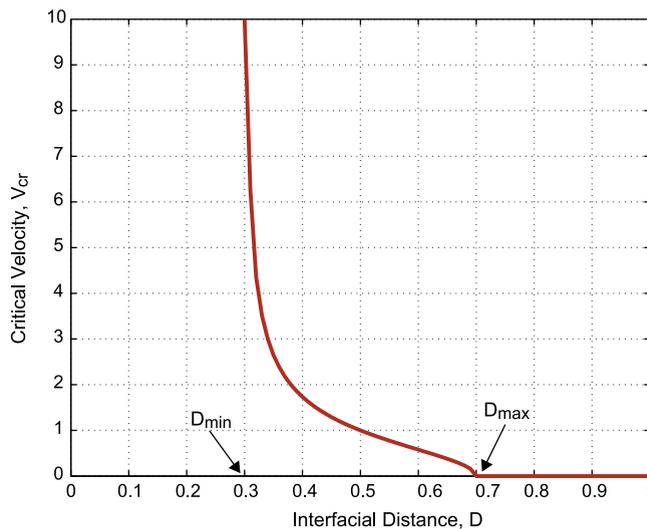
Fig. 6. Variation of the critical velocity V_{cr} as defined by Eq. (2.16). For purpose of illustration, Eq. (2.16) has been plotted for $\zeta = 1, D_{min} = 3/10$ and $D_{max} = 7/10$.
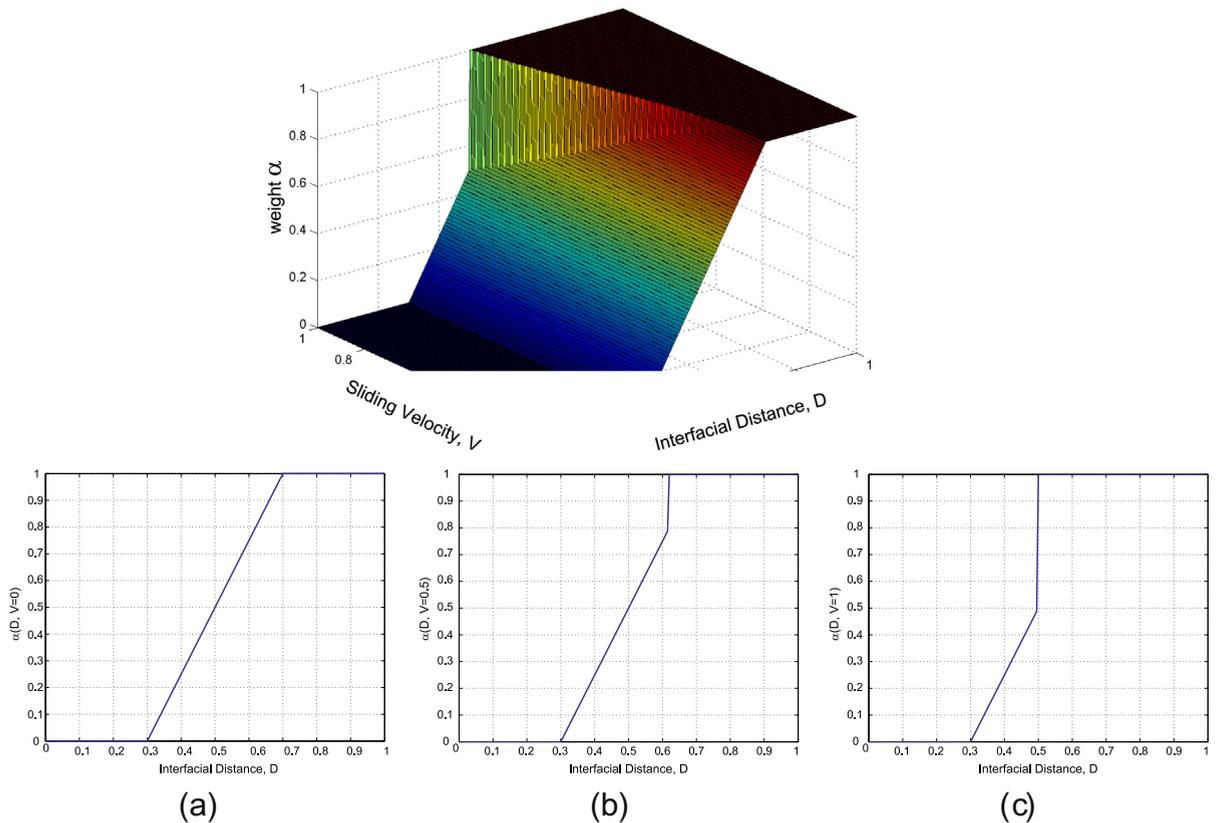
Fig. 7. Graph of the function α as given by Eq. (2.15), along with the cross sections for: (a) $V = 0$; (b) $V = 0.5$; and (c) $V = 1$. For purpose of illustration, Eq. (2.15) has been plotted for $\zeta = 1, D_{min} = 3/10$ and $D_{max} = 7/10$.

(2.15) implies that: (i) the pure frictional behaviour ($\alpha = 0$) will occur when $D \leqslant D_{min}$ for any value of the sliding velocity $|\mathcal{L}_v g_T|$; (ii) the pure viscous behaviour ($\alpha = 1$) is obtained when $D \geqslant D_{max}$ for any value of $|\mathcal{L}_v g_T|$, or when, for any given $D > D_{min}$, there holds $|\mathcal{L}_v g_T| > V_{cr}(D)$; (iii) the mixed lubrication regime ($\alpha \in]0, 1[$) will occur for the other combinations of $|\mathcal{L}_v g_T|$ and D. Fig. 7 displays the graph of $\alpha(|\mathcal{L}_v g_T|, D)$.

For completeness, the total nominal normal pressure can then be computed as follows:

$$t_N = \begin{cases} t_{N,DF}^{nom} & \text{for } D/\sigma_s \leqslant R_1, \\ \dfrac{t_{N,DF}^{nom}(D/\sigma_s)}{\alpha(D/\sigma_s, |\mathcal{L}_v g_T|)} & \text{for } R_1 \leqslant D/\sigma_s \leqslant R_3, \\ t_{N,HL}^{nom} & \text{for } D/\sigma_s \geqslant R_3, \end{cases} \qquad (2.17)$$

where $R_1 = D_{min}/\sigma_s$ and $R_3 = D_{max}/\sigma_s$.

2.6. Evaluation of ζ

The assumption here is that one knows the Stribeck curve or the boundary lubrication map for the tribological system that one is considering. As already mentioned beforehand, such curves can be obtained either from experiments or through the use of microscale models of the contact interface such as in [10,26,28,25]. In the following the boundary lubrication map discussed in [2] is used as point of case. This map displays the tangential force as function of the sliding velocity and is parameterized with respect to the lubricant thickness D. A typical behaviour is displayed in Fig. 8, adapted from [2], where one must identify the points (V_i, D_i) corresponding to the transition to the FHL regime, and the values of D_{max} and D_{min}. For the points marked in Fig. 8, observe that, as expected, as D_i increases, V_i decreases. The parameter ζ is then obtained by the best fit of the function (2.16) to such experimental data.
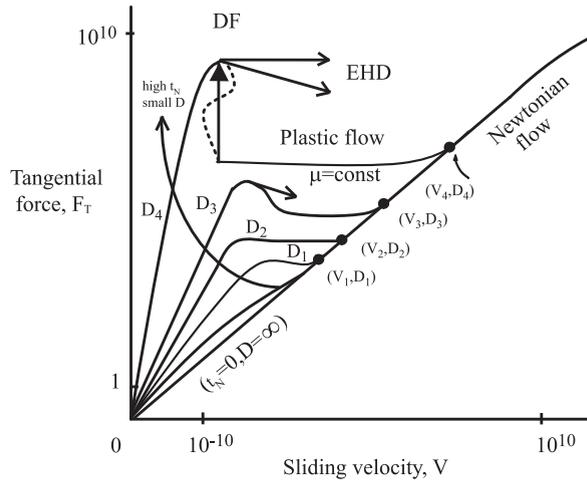
Fig. 8. Boundary lubrication map adapted from [2] with indication of the points (V_i, D_i) for the evaluation of ζ.

2.7. Tangential stress: Evaluation of $\boldsymbol{t}_{T,DF}$

For the evaluation of the dry friction component of the tangential stress, any solid friction law, describing the friction between the solid asperities, can be used. Here, a rate-and-state friction constitutive equation [43–45] has been considered within the framework of non-associative plasticity [46]. Following a standard formalism, the additive decomposition of the total slip g_T is adopted,

$$g_T = \int_{t_s}^{t} \left(\dot{\xi}^{e,\alpha} + \dot{\xi}^{p,\alpha} \right) \tau_\alpha d\tau = g_T^e + g_T^p \tag{2.18}$$

and a state variable θ introduced, which accounts for the current state of the interface. The tangential stress $\boldsymbol{t}_{T,DF}$ is assumed to be proportional to $t_{N,DF}$ but, at variance of Coulomb friction law, the friction coefficient μ depends on the plastic slip rate $\mathcal{L}_v g_T^p$ and on the state variable θ. The resulting slip criterion is then given by

$$\mathcal{F} = |t_{T,DF}| - \mu(\mathcal{L}_v g_T^p, \theta) t_{N,DF}, \tag{2.19}$$

where μ is taken to be of the following form

$$\mu(\mathcal{L}_v g_T^p, \theta) = f(\mathcal{L}_v g_T^p, \theta) \mu_0(\mathcal{L}_v g_T^p). \tag{2.20}$$

The term $f(\mathcal{L}_v g_T^p, \theta)$ is introduced in order to have a creep alike behaviour for μ, as shown by experiments initially carried out on rock friction [43], and subsequently on the contact between different surfaces [47–50]. Such creep behaviour is attributed to the complex dynamics of the interfacial asperities on the microscale [47,51]. By assuming for $f(\mathcal{L}_v g_T^p, \theta)$ the expression

$$f(\mathcal{L}_v g_T^p, \theta) = 1 + m \ln \left(1 + \theta \frac{|\mathcal{L}_v g_T^p|}{D_0} \right), \tag{2.21}$$

and for the evolution of the state variable θ the equation

$$\dot{\theta} = 1 - \theta \frac{|\mathcal{L}_v g_T^p|}{D_0}, \tag{2.22}$$

one can note that a change of $\mathcal{L}_v g_T^p$ induces a delay in μ for the attainment of the corresponding value. The delay depends on the evolution of θ and is controlled by the constants m and D_0, with D_0 the internal length over which $\boldsymbol{t}_{T,DF}$ varies in response to changes of $\mathcal{L}_v g_T^p$, whereas m controls the rate of this change.

The term $\mu_0(\mathcal{L}_v g_T^p)$ models the steady-state friction coefficient; for $\mathcal{L}_v g_T^p$ constant, and $t \to \infty$, from (2.22) one obtains $\theta \to D_0/|\mathcal{L}_v g_T^p|$, so that $\mu(\mathcal{L}_v g_T^p, \theta) \to \mu_0(\mathcal{L}_v g_T^p))$. The term μ_0 is modelled by the following function, displayed in Fig. 9,

$$\mu_0 = \begin{cases} \mu_k + (\mu_s - \mu_k) \exp \left(1 + \frac{A_v^2}{\langle |\mathcal{L}_v g_T^p| - D_0/\tau_0 \rangle_+^2 - A_v^2} \right) & \text{if } |\mathcal{L}_v g_T^p| \leqslant A_v + D_0/\tau_0, \\ \mu_k & \text{otherwise,} \end{cases} \tag{2.23}$$
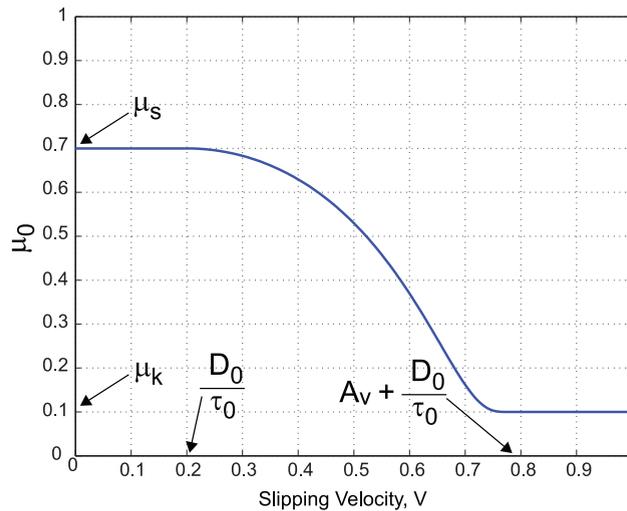
Fig. 9. Variation of the coefficient μ_0 as given by Eq. (2.23). The sliding velocity has been referred here to as slipping velocity to strengthen that V is the plastic slip rate, that is, $V = |\mathcal{L}_v g_T^p|$.

with μ_s and μ_k the static and kinetic friction coefficients, respectively, and τ_0 the characteristic time, introduced in [52,53], over which, on average, the microcontacts are refreshed. The parameter A_v denotes the value of the velocity at which μ_0 attains the kinetic value μ_k. The constitutive model is completed by introducing an 'elasto-perfect plastic' type regularization of the friction law, corresponding to (2.18), with

$$t_{T,DF} = K_T g_T^e \tag{2.24}$$

and by giving the loading/unloading conditions in the standard Kuhn–Tucker form

$$\mathcal{F} \leqslant 0, \quad \dot{\lambda}\mathcal{F} = 0, \quad \dot{\lambda} \geqslant 0. \tag{2.25}$$

Remark 2.4. The parameter K_T that enters (2.24) has the meaning of a penalty factor [14] that has been introduced to regularize the multivalued structure of the Coulomb-like friction law for the computation of $\boldsymbol{t}_{T,DF}$. □

Remark 2.5. At variance of the Dieterich–Ruina model [43,44], the expression of $\mu(V, \theta)$ given by Eq. (2.20) is defined also for vanishing values of the sliding velocity V. Such expression for $\mu(V, \theta)$ has also been considered in [50]. A different expression for describing low-velocity friction, used in forming processes, has instead been given in [54] in the form

$$\mu = a\,\mathrm{asinh}\left[\frac{V}{2V_0}\exp\left(\frac{\mu_0 + b\ln(V_0\theta/D_0)}{a}\right)\right], \tag{2.26}$$

where the parameters a, b, V_0 and μ_0 have the same meaning as in the Dieterich-Ruina model. By inspection of the Dieterich-Ruina model [43,44], of Eq. (2.20) and of Eq. (2.26) the following observations can be drawn: as $V \to 0$, the Dieterich-Ruina model is not defined; Eq. (2.26) as $V \to 0$ delivers $\mu \to 0$; the expression (2.20), considered in this paper, gives as $V \to 0, \mu \to \mu_s$. In this case, one realizes also for $V = 0$ a logarithmic dependence of μ with the time, as confirmed by experiments in [50,55,56], while for the Dieterich-Ruina model this behaviour is related only to $V \neq 0$. □

Remark 2.6. Also in [7] it is recognized the breakdown of the Dieterich-Ruina friction model for vanishing sliding velocity, making it not suitable for forming processes. A different rate-and-state friction law is therein proposed, which is well defined as $V \to 0$ and gives a finite value different from zero. □

2.8. Tangential stress: Evaluation of $\boldsymbol{t}_{T,HL}$

The tangential stress applied by the lubricant in the full hydrodynamic condition is given by

$$t_{T,HL} = \eta_b \mathcal{L}_v g_T/D, \tag{2.27}$$

corresponding to a Newtonian viscous material, where $\mathcal{L}_v g_T / D$ denotes the shear strain rate. Note that $\boldsymbol{t}_{T,HL}$ enters (2.8) with α, hence from (2.15), one has that for $D \leqslant D_{min}$, $\alpha \boldsymbol{t}_{T,HL} = 0$, and this holds also for $D \to 0$. Furthermore, it is worth noting that (2.27) accounts for only the lubricant shearing due to the relative motion of the surfaces, while it neglects the geometric tangential action, due to variation of D, and the so-called rolling action, due to variation of the normal pressure. This approximation is generally acceptable for smooth plane surfaces [13].

For convenience, the basic equations defining the initial value constitutive problem for the contact interface are summarized in Box 1.

Box 1 Initial value constitutive problem for the contact interface

$$\alpha = \begin{cases} \min\left(\frac{\langle D - D_{min}\rangle_+}{D_{max} - D_{min}}, 1\right) & \text{if } |\mathcal{L}_v g_T| < V_{CR}(D), \\ 1 & \text{if } |\mathcal{L}_v g_T| \geqslant V_{CR}(D), \end{cases};$$

$$t_{N,DF}^{nom} = \frac{2}{3} n \beta \sigma_s \sqrt{\frac{\sigma_s}{\beta}} E' \frac{1}{\sqrt{2\pi}} \int_{D/\sigma_s}^{R_3} \left(s - \frac{D}{\sigma_s}\right)^{3/2} \exp\left(-\frac{s^2}{2}\right) ds + K_N \langle -D\rangle_+, \qquad \text{for } D/\sigma_s \leqslant R_3,$$

$$t_{N,HL}^{nom} = \delta \eta_b \frac{|\mathcal{L}_v g_T|}{D} \text{ for } D/\sigma_s \geqslant R_3,$$

$$t_N = \begin{cases} t_{N,DF}^{nom} & \text{for } D/\sigma_s \leqslant R_1, \\ \frac{t_{N,DF}^{nom}(D/\sigma_s)}{\alpha(D/\sigma_s, |\mathcal{L}_v g_T|)} & \text{for } R_1 \leqslant D/\sigma_s \leqslant R_3, \\ t_{N,HL}^{nom} & \text{for } D/\sigma_s \geqslant R_3. \end{cases}$$

$$g_T = g_T^e + g_T^p,$$

$$\boldsymbol{t}_{T,DF} = K_T g_T^e,$$

$$\mathcal{L}_v g_T^p = \dot{\lambda} \frac{\boldsymbol{t}_{T,DF}}{|\boldsymbol{t}_{T,DF}|},$$

$$\mathcal{F} = |\boldsymbol{t}_{T,DF}| - \mu(\mathcal{L}_v g_T^p, \theta) t_{N,DF}^{nom} \leqslant 0, \quad \dot{\lambda} \geqslant 0 \quad \dot{\lambda} \mathcal{F} = 0,$$

$$\mu(\mathcal{L}_v g_T^p, \theta) = f(\mathcal{L}_v g_T^p, \theta) \mu_0(\mathcal{L}_v g_T^p),$$

$$f(\mathcal{L}_v g_T^p, \theta) = a \left[1 + m \ln\left(1 + \theta \frac{|\mathcal{L}_v g_T^p|}{D_0}\right)\right],$$

$$\mu_0 = \begin{cases} \mu_k + (\mu_s - \mu_k) \exp(1 + \frac{A_v^2}{\langle |\mathcal{L}_v g_T^p| - D_0/\tau_0 \rangle_+^2 - A_v^2}) & \text{if } |\mathcal{L}_v g_T^p| \leqslant A_v + D_0/\tau_0, \\ \mu_k & \text{otherwise,} \end{cases}$$

$$\dot{\theta} = 1 - \theta \frac{|\mathcal{L}_v g_T^p|}{D_0},$$

$$\boldsymbol{t}_{T,HL} = \eta_b \mathcal{L}_v g_T / D,$$

$$\boldsymbol{t}_T = (1 - \alpha) t_{T,DF} + \alpha t_{T,HL}.$$

---

3. Numerical integration algorithm

For the numerical integration of the constitutive equations presented in Section 2, the major difficulty lies in the integration of the constitutive relations modelling the tangential action of the dry friction component. The evaluation of the normal contact pressure, on the other hand, is obtained by simply performing a function evaluation, given that both $t_{N,DF}$ and $t_{N,HL}$ have been assumed to depend on the current value of the primary variable with no dependence on the contact interface history. Given, however, the similarity of the dry-friction formulation to rate-independent plasticity, the numerical techniques
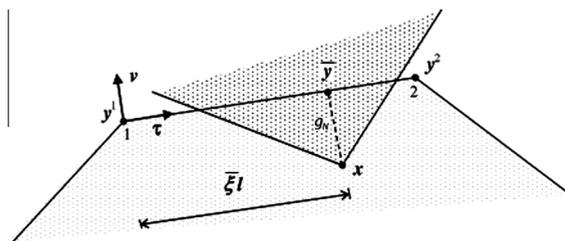
Fig. 10. Node-to-segment discretization of the contact interface.

employed in classical plasticity can be suitably applied. As a result, also here an operator splitting algorithm is employed. In the predictor step only the elastic-type relations are considered, whereas in the corrector step the rate equations, which are approximated by a one step backward Euler scheme, are solved taking the results of the predictor step as the initial conditions. This section gives the algorithmic details for the implementation into the FE code STAMPACK® [57] used to perform the numerical simulations in Section 4. Since the equations of the motion of the two bodies in contact are solved in this code by an explicit scheme [17,18,58,19], only the procedure for the update of the stresses, for the evaluation of the forces through the interface element, is necessary and therefore is herein illustrated.

3.1. The incremental constitutive value problem

For the geometric discretization of the 2d contact interface, the node-to-segment approach has been adopted. This relies on the introduction of the master–slave concept in the current configuration. Fig. 10 displays the node-to-segment contact element with the corresponding geometrical quantities. The kinematical variables are computed by assuming that each discrete slave node x, comes into contact with the master segment 1–2 with end nodes y^1 and y^2. The master segment is then parametrized by the convective coordinates ξ. The gap distance g_N and the tangent vector can also be computed. For the full details of this approach, one can refer to [34] Chapter 9 and the references therein. Within the displacement driven solution of the contact problem, associated with an active set strategy to define the active contact constraints, the state of the contact interface at t_n and the incremental variables Δg_{n+1} and $\Delta g_{T,n+1}$, are assumed to be known at the point $\bar{y}$. To update the interface state at t_{n+1}, one needs to identify first the type of lubrication regime that occurs. This is achieved by evaluating α_{n+1} through (2.15), with D_{n+1} computed in terms of g_{n+1}, and $\mathcal{L}_v g_T|_{n+1}$ computed by finite difference approximation of (2.3), i.e.

$$\mathcal{L}_v g_T|_{n+1} \approx \frac{\Delta g_{T,n+1}}{\Delta t} = \frac{(\bar{\xi}^\beta_{n+1} - \bar{\xi}^\beta_n)}{\Delta t} \tau_{\beta, n+1}. \tag{3.1}$$

If $\alpha_{n+1} = 1$, the full hydrodynamic conditions are realized, with a pure viscous behaviour of the interface, that is, $t^{n+1}_{N,DF} = 0$ and $\boldsymbol{t}^{n+1}_{T,DF} = 0$, while $t^{n+1}_{N,HL}$ and $\boldsymbol{t}^{n+1}_{T,HL}$ are obtained from (2.14) and (2.27), respectively, using the approximation (3.1). If $\alpha_{n+1} < 1$, the dry-friction component needs also to be evaluated by solving the following system of nonlinear algebraic equations:

$$
\left|
\begin{array}{ll}
\textbf{Given :} & g_{T,n}, \ g^p_{T,n}, \ \theta_n, \ \lambda_n, \\[4pt]
& \Delta g_{T,n+1}, \\[8pt]
\textbf{Find :} & g^e_{T,n+1}, \ \Delta g^p_{T,n+1}, \ \theta_{n+1}, \ \Delta\lambda, \ t^{n+1}_{T,DF}, \\[6pt]
& g_{T,n+1} = g^p_{T,n} + \Delta g^p_{T,n+1} + g^e_{T,n+1}, \quad (a) \\[6pt]
& t^{n+1}_{T,DF} = K_T g^e_{T,n+1}, \quad\quad (b) \\[8pt]
\textbf{Such that :} & \theta_{n+1} = \theta_n + \Delta t\left(1 - m\frac{\theta_{n+1}}{D_0}\frac{|\Delta g^p_{T,n+1}|}{\Delta t}\right), \quad (c) \\[10pt]
& \Delta g^p_{T,n+1} = \Delta\lambda \frac{t^{n+1}_{T,DF}}{|t^{n+1}_{T,DF}|}, \quad (d) \\[10pt]
& \mathcal{F}_{n+1} < 0, \quad \Delta\lambda > 0, \quad \Delta\lambda\mathcal{F}_{n+1} = 0, \quad (e)
\end{array}
\right.
\tag{3.2}
$$

where

$$\mathcal{F}_{n+1} = |t^{n+1}_{T,DF}| - \mu_{n+1} t^{n+1}_N \tag{3.3}$$

and

$$\mu_{n+1} = f\left(\theta_{n+1}, \frac{\Delta g^p_{T,n+1}}{\Delta t}\right)\mu_0\left(\frac{\Delta g^p_{T,n+1}}{\Delta t}\right), \tag{3.4}$$

with the functions f and μ_0 given by (2.21) and (2.23), respectively, whereas $t^{n+1}_{N,DF}$ is obtained from (2.13) in terms of the given g_{n+1}.

Remark 3.1. In applying Eq. (2.9) to compute $t_{N,DF}^{n+1}$, the assumption $D_{n+1} = g_{n+1}$ will be made. This means that the surface roughness profile is assumed to be rigid. Eq. (2.9) will be, therefore, applied at the different time instants t_n with the values of n, β and σ_s characterizing the initial surface roughness. A rigorous evaluation of $t_{N,DF}$ should rather account for the surface roughness with the deformation. For a more detailed discussion on this subject, one can refer to [24] where such influence has been nevertheless analysed for the deformations produced by the lubricant pressure. □

3.2. The dry-friction traction update algorithm

For the solution of (3.2), a predictor–corrector scheme can be used, as illustrated in [34]. In the predictor step, one sets the trial $\Delta g_{T,n+1}^p = \mathbf{0}$, i.e. one assumes stick condition, and evaluates the elastic trial traction

$$t_{T,DF}^{n+1,trial} = K_T(g_{T,n+1} - g_{T,n}^p) \tag{3.5}$$

and the friction criterion

$$\mathcal{F}_{n+1}^{trial} = |t_{T,DF}^{n+1,trial}| - \mu_{n+1}^{trial} t_{N,DF}^{n+1}, \tag{3.6}$$

where from (2.20), (2.21) and (2.23) one obtains

$$\mu_{n+1}^{trial} = \mu_s. \tag{3.7}$$

If $\mathcal{F}_{n+1}^{trial} \leqslant 0$, the elastic trial state with

$$t_{T,DF}^{n+1} = t_{T,DF}^{n+1,trial}, \quad \Delta\lambda = 0, \quad \Delta g_{T,n+1}^p = \mathbf{0} \text{ and } \theta_{n+1} = \theta_n + \Delta t \tag{3.8}$$

is solution of (3.2), otherwise one needs to compute the corrected state by projecting $t_{T,DF}^{n+1,trial}$ onto the friction criterion. In turn, this means to find $\Delta g_{T,n+1}^p$ so that $\mathcal{F}_{n+1} = 0$ is met, with $\mathcal{F}_{n+1}$ expressed below in terms of the only scalar $\Delta\lambda$. Following standard arguments on the return mapping algorithm [59,60], Eq. (3.2)(b) can be re-written as

$$t_{T,DF}^{n+1} = t_{T,DF}^{n+1,trial} - K_T\Delta\lambda \frac{\mathbf{t}_{T,DF}^{n+1}}{|t_{T,DF}^{n+1}|} \tag{3.9}$$

which, for $\Delta\lambda > 0$, yields

$$|t_{T,DF}^{n+1,trial}| = |t_{T,DF}^{n+1}| + K_T\Delta\lambda \tag{3.10}$$

and

$$\frac{\mathbf{t}_{T,DF}^{n+1}}{|t_{T,DF}^{n+1}|} = \frac{\mathbf{t}_{T,DF}^{n+1,trial}}{|t_{T,DF}^{n+1,trial}|}. \tag{3.11}$$

Since there holds

$$|\Delta g_{T,n+1}^p| = \Delta\lambda, \tag{3.12}$$

one can explicitly solve θ_{n+1} with respect to $\Delta\lambda$ by using (3.2)(c) which gives

$$\theta_{n+1} = \frac{\theta_n + \Delta t}{1 + \frac{\Delta t \Delta\lambda}{D_0}}. \tag{3.13}$$

This expression, replaced into (2.21), along with (2.23), permits μ_{n+1} to be expressed in terms of only $\Delta\lambda$, so that the condition $\mathcal{F}_{n+1} = 0$ reads as

$$\mathcal{F}_{n+1}(\Delta\lambda) = |t_{T,DF}^{n+1,trial}| - K_T\Delta\lambda - \left[1 + m\ln\left(1 + \frac{\theta_n + \Delta t}{1 + \frac{\Delta t \Delta\lambda}{D_0}}\frac{\Delta\lambda}{D_0}\right)\right]\mu_0(\Delta\lambda)t_{N,DF}^{n+1} = 0. \tag{3.14}$$

The solution of (3.14), obtained by applying, for instance, Newton's method, allows one then to compute the frictional slip $\Delta g_{T,n+1}^p$ from

$$\Delta g_{T,n+1}^p = \Delta\lambda \frac{t_{T,DF}^{n+1,trial}}{|t_{T,DF}^{n+1,trial}|} \tag{3.15}$$

and to obtain the traction update from (3.9) after accounting for (3.11).

The complete algorithm is summarized in Box 2.

Box 2. Numerical Integration Algorithm

Given :
$$g_{T,n}, \ g_{T,n}^p, \ \theta_n, \ \lambda_n,$$
$$g_{n+1}, \ \Delta g_{T,n+1}, \ \Delta t,$$

Compute :
$$\alpha\left(g_{n+1}, \frac{\Delta g_{T,n+1}}{\Delta t}\right) \text{ from Eq. 2.15,}$$
$$t_{N,HL}^{n+1} = \eta \frac{|\Delta g_{T,n+1}|}{\Delta t D}, \quad t_{T,HL}^{n+1} = \eta_b \frac{\Delta g_{T,n+1}}{\Delta t},$$
$$\alpha = 1,$$

IF
$$t_{N,DF}^{n+1} = 0, \quad t_{T,DF}^{n+1} = \mathbf{0},$$
$$\lambda_{n+1} = \lambda_n, \quad g_{T,n+1}^p = g_{T,n}^p, \quad \theta_{n+1} = \theta_n + \Delta t,$$

$t_{N,DF}^{n+1}$ from Eq. 2.13 with $D_{n+1} = g_{n+1}$,

−**Predictor step**
$$t_{T,DF}^{trial,n+1} = K_T(g_{T,n+1} - g_{T,n}^p),$$

−**Check for slip criterion**
$$\mathcal{F}_{n+1}^{trial} = |t_{T,DF}^{n+1,trial}| - \mu_s t_{N,DF}^{n+1},$$

IF$\mathcal{F}_{n+1}^{trial} \leqslant 0$,
$$t_{T,DF}^{n+1} = t_{T,DF}^{n+1,trial}, \quad \Delta\lambda = 0, \quad \Delta g_{T,n+1}^p = \mathbf{0}, \quad \theta_{n+1} = \theta_n + \Delta t,$$

ELSE   **ELSE**

−**Corrector step**

Solve for$\Delta\lambda : \mathcal{F}_{n+1}(\Delta\lambda) = 0$ from Eq. 3.14

$$\Delta g_{T,n+1}^p = \Delta\lambda \frac{\mathbf{t}_{T,DF}^{n+1,trial}}{|t_{T,DF}^{n+1,trial}|},$$

$$t_{T,DF}^{n+1} = t_{T,DF}^{n+1,trial} - K_T\Delta\lambda \frac{\mathbf{t}_{T,DF}^{n+1,trial}}{|t_{T,DF}^{n+1,trial}|},$$

$$\theta_{n+1} = \frac{\theta_n + \Delta t}{1 + \frac{\Delta t \Delta\lambda}{D_0}},$$

END

END   **END**

4. Numerical examples

Three numerical examples are presented in this section. In the first two examples, the dry friction and the lubricated contact component of the constitutive contact model are tested separately, by looking at the contact between an elastomer and a

Table 1
Parameters used to characterize the roughness of the elastomer contact surface (values taken from [26]).

n, [m^{-2}]	β [m]	σ_s [m]	E' [N/m^2]
$2.5 \cdot 10^{10}$	$10 \cdot 10^{-6}$	$0.2 \cdot 10^{-6}$	$1.5 \cdot 10^{11}$
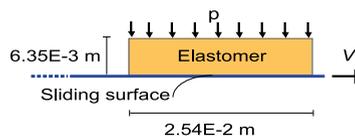
Fig. 11. Model problem for an elastomer sliding on a hard smooth surface (glass).

Table 2
Input parameters for the Ogden hyperelastic model.

α_1	μ_1 [N/m^2]	α_2	μ_2 [N/m^2]	α_3	μ_3 [N/m^2]	K [N/m^2]
1.3	$6.3 \cdot 10^6$	5.0	$1.3 \cdot 10^4$	−2.0	$-1.0 \cdot 10^5$	$1.0 \cdot 10^9$

Table 3
Input parameters for the contact model.

μ_s	μ_k	A_v [m/s]	$A_v + D_0/\tau_0$ [m/s]
2.5	0.3	$1 \cdot 10^{-3}$	2.5
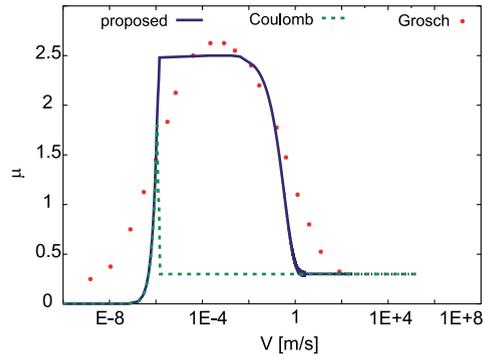
Fig. 12. Variation of the friction coefficient with the sliding velocity for the contact conditions of dry friction between an elastomer and a smooth surface. The experimental results are taken from [61].
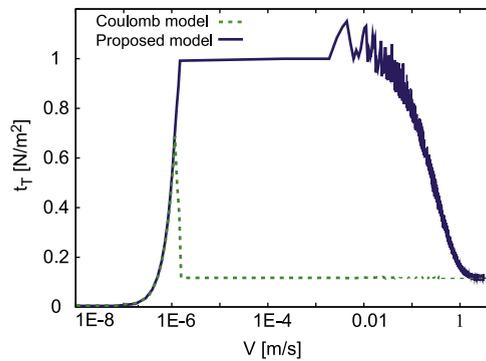
Fig. 13. Variation of the tangential stress t_T versus the sliding velocity V.

smooth surface. Such pair of contacting surface represents the tribological system used in the third example which reports on the numerical simulation, in the cosmetic industry, of the stamping of a ridge on an aluminum tube using the technique of the hydroforming process with an elastomer as pressure medium. Comparisons with the process that uses the fluid pressure medium are also made.

4.1. Dry friction between an elastomer and a smooth surface

In this section, the sliding between an elastomer and a slightly wavy glass surface. in dry conditions is analysed. The elastomer is assumed to have a rough flat interface with roughness of Gaussian type characterized by the values listed in Table 1, whereas the glass surface is assumed to be smooth. The FE model used for the numerical simulations is shown in Fig. 11. Plane strain conditions are assumed. The elastomer is discretized using plane strain quadrilateral elements with four Gauss points for the numerical integration, whereas the glass is modelled by line elements, wherein the dry friction contact conditions are imposed.

For the elastomer, a quasi-incompressible hyperelastic material model with the following Ogden type strain energy has been used

$$\Psi = \sum_{p=1}^{3} \frac{\mu_p}{\alpha_p} \left(\bar{\lambda}_1^{\alpha_p} + \bar{\lambda}_2^{\alpha_p} + \bar{\lambda}_3^{\alpha_p} - 3 \right) + \frac{1}{2} K(J-1)^2, \qquad (4.1)$$
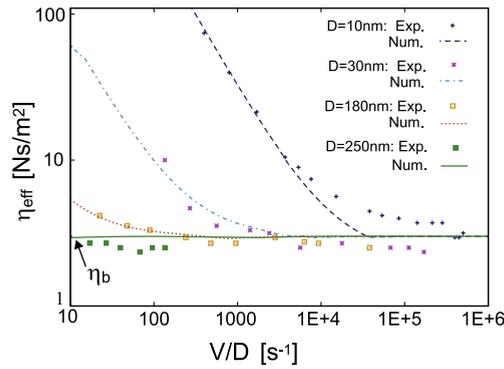
Fig. 14. Variation of the effective viscosity $\eta_{eff} = t_T D/V$ with respect to the shear strain rate V/D for different lubricant thicknesses.
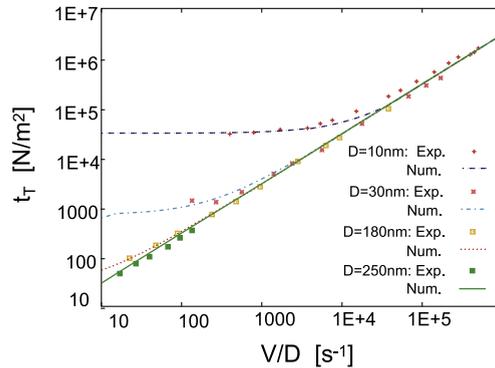
Fig. 15. Variation of the tangential contact stress with respect to the shear strain rate V/D for different lubricant thicknesses.

where λ_i, for $i = 1, 2, 3$, are the singular values of the deformation gradient $F = \nabla\varphi$, i.e. $\lambda_i = \sqrt{\text{eig}(F^T F)}, J = \lambda_1\lambda_2\lambda_3$, and $\bar{\lambda}_i = \lambda_i/J^{1/3}$. The parameter K and (α_p, μ_p), for $p = 1, 2, 3$ are material constants given in Table 2, whereas Table 3 reports the material parameters used to define the rate-and-state equation describing the dry friction component of the contact model.

For comparison, also the classical Coulomb friction law with the following values of the friction coefficient $\mu_S = 2.5$ and $\mu_K = 0.3$ has been implemented. The values used for the static and kinetic friction coefficient are taken from the experimental results obtained originally by Grosch [61] for rubber sliding on polished stainless steel, and reproduced lately by Barquins & Roberts in [62] and Pinnington in [63]. Such experiments show that the rubber friction coefficient increases with the sliding speed and the surface smoothness. The viscoelastic properties of the rubber also influence its frictional behaviour and two distinct source of friction can be observed: the first one originates from interfacial adhesion, which is the only source of friction present between smooth surfaces; the second one is due to the energy losses arising from the deformation of the rubber surface by the surface asperities. All these mechanisms are summarized in the all-one Coulomb friction coefficient.

The rubber element and the sliding surface are initially in contact with a constant pressure p applied to the rubber, whereas the lower flat surface is subjected to a linear increasing velocity V.

The values of μ computed with the proposed model and the Coulomb friction law are displayed in Fig. 12, as a function of the sliding velocity V. For comparison, the experimental values of μ, taken from [61], have also been reported. The examination of the numerical results with the new contact model show that one can identify three type of variations: In the first one, the coefficient μ increases up to a value equal to 2.5, which coincides with μ_s. Such value of μ remains then constant as V increases up to the critical value A_v. At such value of V, μ starts to decrease. For the decreasing branch, the inspection of Fig. 13, which displays the concomitant variation of the tangential stress t_T, shows oscillations in the values of t_T. These oscillations were seen from the computation to be due to a sequence of stick ($\Delta g_T^p = 0$) and slip ($\Delta g_T^p \neq 0$) steps, as a result of oscillations in the corresponding values of the normal pressure t_N. These, in turn, arise because of the softening of the constitutive law $\mu = \mu(V)$. In the third phase, which occurs when V crosses the value $A_v + D_0/\tau_0$, the coefficient μ attains the constant value μ_k. At variance of the Coulomb friction law, the proposed model correlates quite well with the experimental results of [61]. Using Coulomb friction, once sliding starts, there is an abrupt change in the value of μ to the value of the kinetic friction coefficient μ_k. Such discontinuity is accompanied by only negligible oscillations of t_T. This behaviour does not reflect, however, what is observed in the experiments [61].
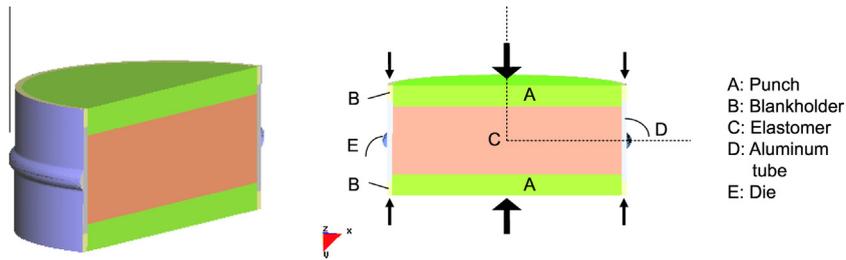
Fig. 16. Stamping tools for the forming process of a ridge with the tube hydroforming technique.
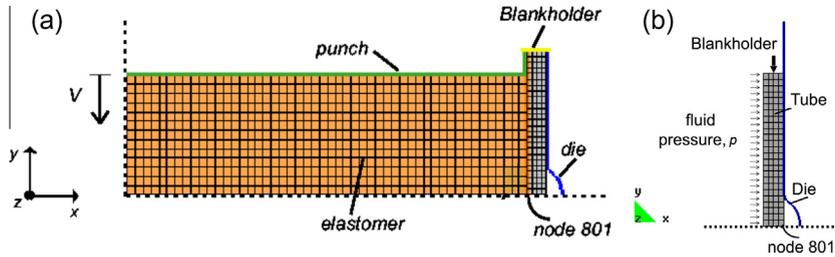
Fig. 17. Finite element model for the stamping of the ridge in the case of (*a*) an elastomer forming process (EF process), and (*b*) the fluid pressure forming process (FPF process).

Table 4
Material constants for the elastomer: (α_1, μ_1) Ogden's parameters; K bulk modulus; τ retardation time which enters the definition of the evolution law for the variables b_e and b_{eq}; $v_{rel} = \mu_1/\mu_{v1} = \alpha_1/\alpha_{v1}$ ratio of the nonviscous to viscous Ogden hyperelastic parameters; σ_y yield stress.

α_1	μ_1 [N/m^2]	K [N/m^2]	τ [s]	v_{rel}	σ_y [N/m^2]
3.10	$1.05 \cdot 10^6$	$1.0 \cdot 10^{10}$	720.0	0.55	$1.2 \cdot 10^6$

Table 5
Model parameters for the contact at the elastomer/tube interface.

μ_s	μ_k	D_0/τ_0 [m/s]	D_0 [m]	m	A_v [m/s]	η_b [Ns/m^2]
0.6	0.1	0.3	$1.0 \cdot 10^{-6}$	$10.0 \cdot 10^{-2}$	2.5	0.3

4.2. Sliding between two lubricated nominally flat surfaces

For the same system depicted in Fig. 11, in this example the lubricated component of the model is tested and compared with the experimental results taken from [2,64]. The finite element model used for the numerical simulations and the loading scheme is the same as the one applied in the previous example, with a normal pressure $p = 3.0E6$ Pa applied to the upper surface and maintained constant throughout the test, while the lower surface is displaced transversally at linear increasing velocity V.

For the setting of this experiment, the data from [2,64] are employed (see Fig. 3 of [2] and Fig. 12 of [64] with correspondent comments). The contact interface is lubricated with a polymer melt polybutadien PBD7000 with $\eta_b = 4$ Ns/m^2 at $T = 28$ °C. The behaviour of the lubricant is assessed for four different values of D, that is, for $D = 10$ nm, $D = 30$ nm, $D = 180$ nm and $D = 250$ nm, whereas D_{max} and D_{min} are taken equal to 250 nm and to 0 nm, respectively. The bulk viscosity η_b is assumed to be constant with temperature and pressure.

In order to compare with the experiments reported in [64], the results of the numerical simulations are displayed in Fig. 14 by plotting, for the different values of D, the effective viscosity η_{eff}, introduced in [2] and defined as $\eta_{eff} = t_T D/V$, with respect to V/D. This representation, referred to as boundary lubrication map in [2], is argued to be more representative of the Stribeck curve.

For $D = 10$ nm and low velocities, from (2.15) one gets that $\alpha = 0.05$, and the interface presents a behaviour that is similar to the one obtained by using the Coulomb friction law with constant μ, given that η_{eff} varies as D/V, i.e. $\eta_{eff} \sim D/V$, which
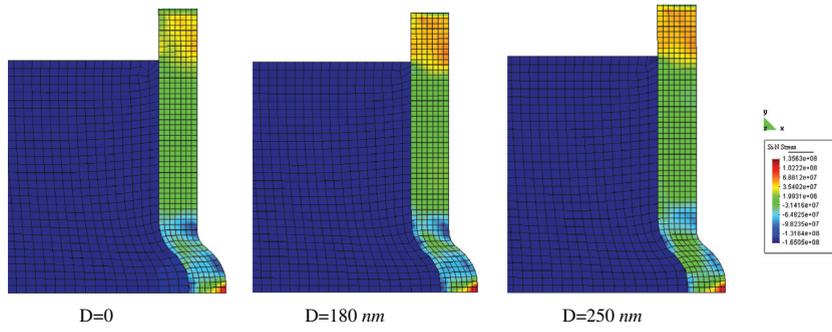
Fig. 18. Maximum principal stresses in the tube produced during the elastomer forming pressure, and for different lubrication thickness: $D = 0$ nm, $D = 180$ nm and $D = 250$ nm.
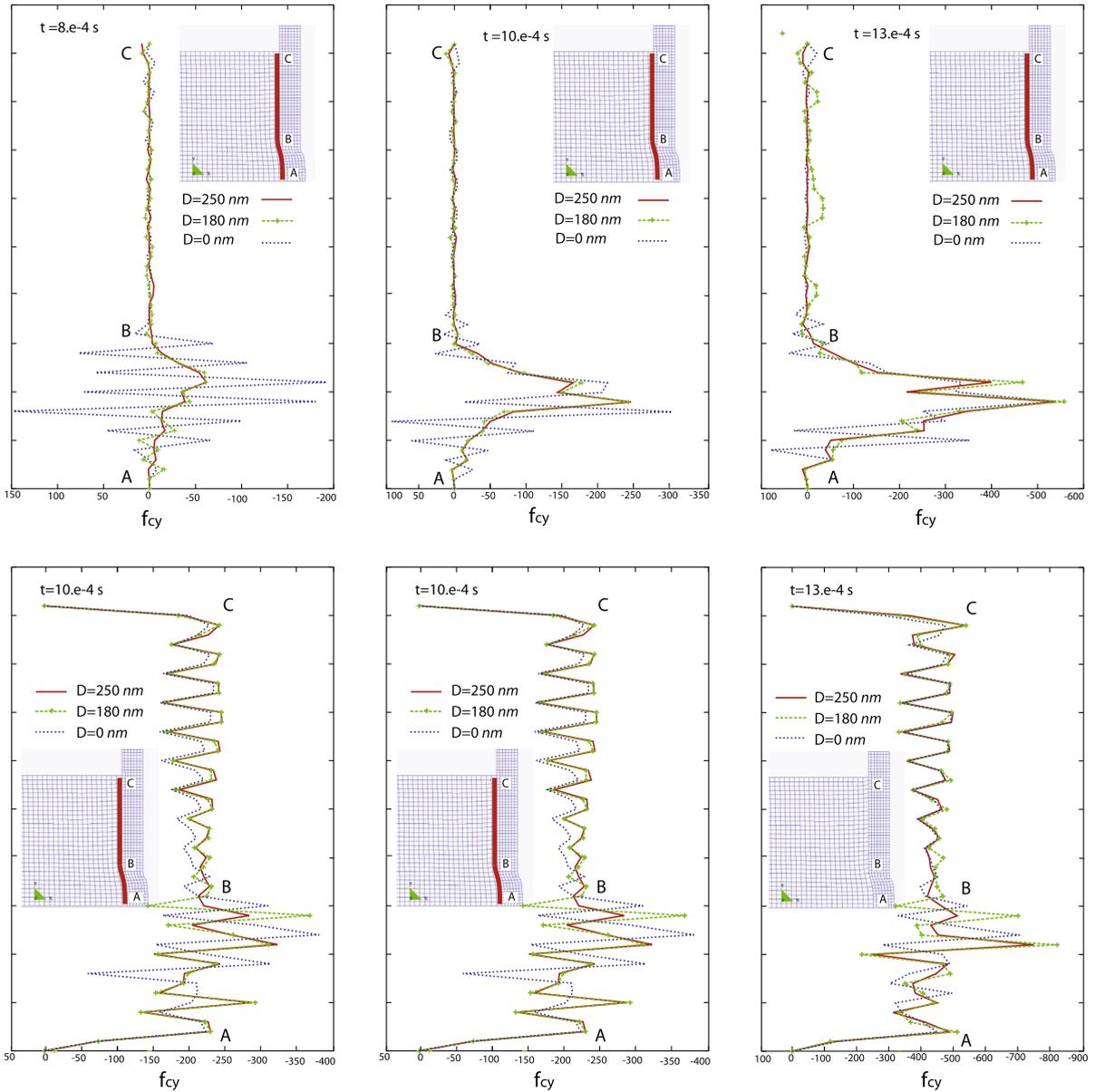
Fig. 19. Contact forces f_{cy} and f_{cx} applied to the nodes of the elastomer-aluminium interface at three time instants: $8.0 \cdot 10^{-4}$ s, $1.0 \cdot 10^{-3}$ s and $1.2 \cdot 10^{-3}$ s and for different lubrication thicknesses.
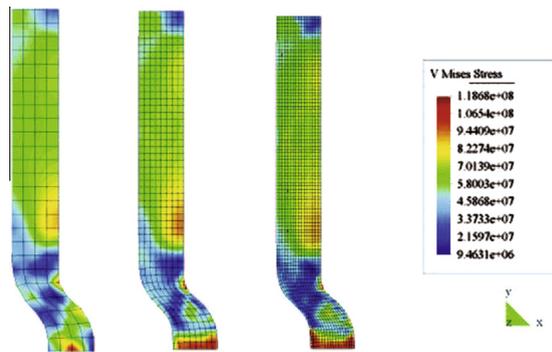
Fig. 20. Maximum principal stresses in the tube produced during the fluid pressure forming process solved with three different meshes for the assessment of the numerical simulation accuracy.
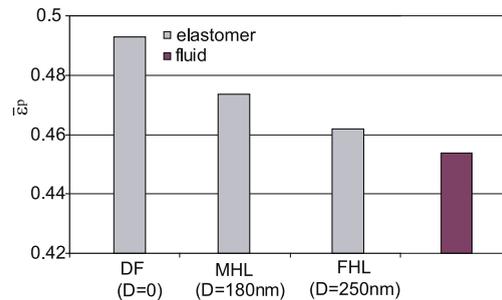
Fig. 21. Maximum effective plastic strain $\bar{\epsilon}^p$ in the metallic tube for the different interface behaviour of the elastomer/tube in the EF process, and in the case of the FPF process, at the time instant $t = 0.17$. Recall that $\bar{\epsilon}^p$ is related to the accumulated plastic strain.

then means that $t_T \sim constant$. As the sliding velocity increases, the effective viscosity η_{eff} decreases until getting the value η_b for $V > V_{cr}(D)$, which corresponds to the realization of the FHL conditions.

For the other values of D, one has, as expected, a shift towards the pure viscous behaviour, in the sense that for values of V lower than the previous case, η_{eff} soon takes on the value η_b, that is, the interface presents a DF and MHL behaviour only for a small range of values of V.

For completeness, the variation of t_T with V/D is displayed in Fig. 15.

4.3. Stamping process of a ridge on an aluminum tube

The hydroforming technology is widely used today in the production of low cost and lightweight components for the automotive, aerospace and household industries compared with traditional forming processes. Among the hydroforming processes, the tube hydroforming technology presents several advantages, such as weight reduction, improved part strength and stiffness, and lower tooling cost [65].

In its simplest scheme, this technology consists of a combined loading of compression forces at the tube ends as well as an hydrostatic internal pressure applied by a viscous medium. These loads expand the tube and lead to the alignment of the tube wall with the outside surface of the die cavity.

Tube hydroforming processes are traditionally realized using a fluid as pressure medium, and only quite recently, the use of elastomer to apply the forming pressure is emerging as a valuable alternative, for reducing the leakage and for an easier handling in the prototype production of small number of parts [66].

In this section the finite element modelling of a ridge on an aluminum tube by the tube hydroforming process is discussed. In the forming process, illustrated in Fig. 16, the two punches are moved at constant velocity against the viscous pressure media that pushes the aluminum tube into the die cavity. In order to ease the forming process, a blankholder applies either a linearly increasing force or is constrained to have the same displacement as the punches. The process completes when the ridge is completely formed and the punches are released to return to their original configuration. The present simulations are performed considering both a polyurethane elastomer with hardness A65 (hereafter, referred to as elastomer forming process, EF process in shorthand) and a fluid as viscous pressure media (hereafter, referred to as fluid pressure forming process, FPF process in shorthand), and their performance is compared.

Given that the hydroformed sections are generally subjected to high thickness variation, it is very important to have the control of the lubrication conditions that determine the actions applied onto the components and the tool surfaces. This is in
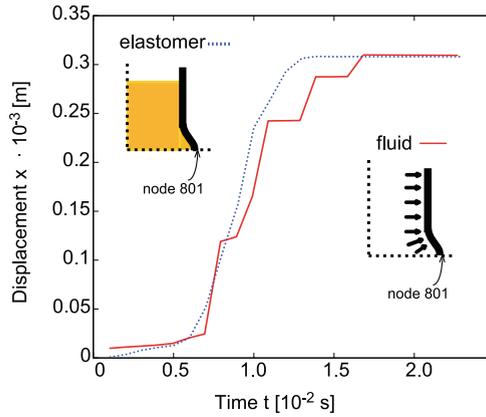
Fig. 22. Comparison of the time history for the displacement along *x* of the node 801 during the elastomer and the fluid pressure forming process.

order to avoid material failures and excessive localized material thinning during the process. Different lubrication thicknesses have therefore been considered in the simulations and carefully analysed.

Fig. 16 shows the geometrical model used in the simulations: Die cavity radius $R_d = 8.635$ mm; Aluminum cylinder inner radius $R_c = 8.235$ mm with thickness $t = 0.38997$ mm; Elastomer radius $R_e = 8.235$ mm. The finite element model is displayed in Fig. 17 where axisymmetric 4–node bilinear isoparametric elements have been used. Fig. 17(a) shows the FE model for the EF process, whereas Fig. 17(b) depicts the FE model for the FPF process. In the FPF process, the fluid pressure is treated as a follower load, and is applied according to a linear time variation up to $p_{max} = 1.55 \cdot 10^8$ N/m². The blankholder load is $P = 10$ N.

In the EF process, because of higher pressures involved, one needs to account for the nonlinear stress–strain response of the elastomer, as well as of its damping, rate–independent hysteresis and quasi–incompressibility. For these reasons, the visco-hyperelastic model with associative plasticity and large deformations developed in [67] has been employed. The model assumes the multiplicative split $F = F_e F_i = F_{eq} F_p$, and, correspondingly, a free Helmhotz energy of the type

$$\Psi = \Psi_{eq}(J^{-2/3}F_{eq}F_{eq}^T) + \Psi_e(J^{-2/3}F_eF_e^T) + \Psi_v(J), \tag{4.2}$$

with, in the case of this example,

$$\Psi_v = \frac{K}{2}(J-1)^2, \quad \Psi_e = \frac{\mu_1}{\alpha_1}\sum_{i=1}^3 \bar{\lambda}_{e,i}^{\alpha_1}, \text{ and } \Psi_{eq} = \frac{\mu_{v1}}{\alpha_{v1}}\sum_{i=1}^3 \bar{\lambda}_{eq,i}^{\alpha_{v1}}, \tag{4.3}$$

with $J = \lambda_1\lambda_2\lambda_3$, λ_i singular values of F, $\lambda_{e,i}$ and $\lambda_{eq,i}$ singular values of F_e and F_{eq}, respectively, and, in general, $\bar{\lambda} = J^{-1/3}\lambda$. Evolution laws also must be given for $b_e = J^{-2/3}F_eF_e^T$ and $b_{eq} = J^{-2/3}F_{eq}F_{eq}^T$; for more details, the work [67] must be referred to. The material constants used for the model, with Von Mises perfect plasticity, are given in Table 4. The aluminum tube has been modelled as an elastic–perfectly plastic material with Prandtl–Reuss evolution law, assuming $E = 6 \cdot 10^{10}$ N/m², $v = 0.33$ and $\sigma_y = 1.20 \cdot 10^8$ N/m².

As for the contact conditions, in the EF process, these must be enforced at the elastomer/tube interface and at the tube/die interface when the ridge starts forming, whereas for the FPF process, the contact conditions must be assigned only at the tube/die interface. The model of this paper has been applied only to describe the elastomer/tube interface with the values listed in Table 5, whereas a Coulomb friction law with $\mu_s = 2.5$ and $\mu_k = 0.01$ has been employed for the tube/die interface in both the processes. The penalty parameters K_N and K_T have been taken both equal to $1 \cdot 10^8$ N/m².

In the simulations, three lubrication thicknesses have been considered for the elastomer/tube interface: $D = 0$ nm, $D = 180$ nm and $D = 250$ nm whereas the values of D_{min} and D_{max} have been taken equal to 0 nm and 250 nm, respectively.

In order to appreciate the importance of the different types of lubrication interfaces in an EF process, Figs. 18 and 19 depict the stress distribution map and the contact forces applied to the nodes of the elastomer-aluminium interface, respectively. The dry friction interface exhibits slightly higher stresses near the ridge, being there the location of higher friction. The contact forces f_{cy} along the *y* direction, which coincides roughly with the direction of the interface, are smoothed with the introduction of the lubricant layer and increase during the forming process. The contact forces f_{cx}, as opposite, do not display sensible variations with the type of interface. The distribution of the maximum principal stresses obtained during the FPF process and with different FE meshes, is also shown in Fig. 20 for the assessment of the accuracy of the simulation. By comparison, the map of the maximum principal stresses produced during the FPF process exhibits slightly lower values, but their distribution is less uniform than that produced during the EF process. As measure of the permanent deformations produced during the two processes, Fig. 21 compares the maximum value of the effective plastic strain $\bar{\epsilon}^p$ in the metallic tube, where $\bar{\epsilon}^p = \sum \sqrt{2/3\Delta\bar{\epsilon}^p : \Delta\bar{\epsilon}^p}$ with the sum over the time increments. While the FPF process produces for $(\bar{\epsilon}^p)_{max}$ a lower value than the one obtained with the EF process, the value produced using the EF process with a FHL interface is

comparable with the one obtained using the FPF process. Finally, the displacement of the node 801, located on the outer surface of the metallic tube that displaces within the die cavity, is used to monitor the evolution of the whole process and to express a qualitative assessment on its regularity. Examination of Fig. 22 shows that the EF process realizes a smoother evolution than the FPF process, given that the latter displays alternate steep displacement variations and large slips.

By conclusion, the FPF process apparently produces lower stresses and lower plastic deformations in the tube, but the corresponding values obtained with the EF process with lubricated interfaces are however comparable, with moreover the additional benefit of realizing a smoother distribution of stresses and smoother process evolution.

5. Summary and Conclusions

A constitutive model for contact interface that accounts for the different lubrication regimes during a forming process, has been proposed in this paper. The model defines the load bearing capacity of the interface as a combination of the solid contact at the asperities and the lubricant action on the wet surfaces. The contribution of each of the two mechanisms is quantified by a constitutive coefficient α that depends on macroscopic state variables, namely the lubricant thickness D and the sliding velocity $\mathcal{L}_v g_T$. The constitutive relation that defines α can be obtained either from an experimental Stribeck curve for the tribological system that one is examining, or from a sequential multiscale analysis where microscale models are used to describe the interface behaviour. In this paper, a simple though effective representation of α has been employed, which is able to capture nevertheless the salient features of a Stribeck curve.

A numerical algorithm for the solution of the initial value constitutive problem has been developed and implemented in an explicit FE code for applications to forming processes. The relevance of the model has been demonstrated by testing some basic tribological systems. The numerical results presented good agreement with experiment. Comparisons with the Coulomb friction law have also been made showing, in the cases that have been examined, the limits of the Coulomb model. A real industrial application for the stamping of a ridge on a metallic tube using the technique of hydroforming has been carried out and used to compare the performance of an elastomer forming process and of the fluid pressure forming process. It was demonstrated that while the FPF process produces lower stresses and lower plastic deformations in the tube, the EF predicts smoother distribution of stresses and a smoother process evolution, so to render the EF a viable alternative to the FPF process.

In summary, the numerical simulations presented in this paper show that for reliable numerical simulation of a forming process, where different lubrication regimes can develop and therefore different type of loads can be applied on the forming piece, the use of contact interface models with more physics are necessary as opposite to the Coulomb friction law, and can be developed with relative ease, at least for first analysis. It is also recognized that the accuracy of the proposed model can be improved, within this same framework, through a more refined definition of the constitutive relation for α by using microscale models. This will be object of future research.

Acknowledgements

References

[1] B.J. Hamrock, S.R. Schmid, B.O. Jacobson, Fundamentals of Fluid Film Lubrication, second ed., Marcel Dekker Inc., New York, 2004.
[2] G. Luengo, J. Israelachvili, S. Granick, Generalized effects in confined fluids: new friction map for boundary lubrication, Wear 200 (1996) 328–335.
[3] F. Martinet, P. Chabrand, Application of ALE finite elements method to a lubricated friction model in sheet metal forming, Int. J. Solids Struct. 37 (2000) 4005–4031.
[4] C. Drummond, J. Israelachvili, Dynamic phase transitions in confined lubricant fluids under shear, Phys. Rev. E 63 (2001). 041506 (pp. 11).
[5] J. Hol, M.V. Cid Alfaro, M.B. de Rooij, T. Meinders, Advanced friction modeling for sheet metal forming, Wear 286–287 (2012) 66–78.
[6] Z. Mrôz, S. Stupkiewicz, Constitutive model of adhesive and ploughing friction in metal-forming processes, Int. J. Mech. Sci. 40 (1998) 281–303.
[7] T.A. Laursen, V.G. Oancea, On the constitutive modeling and finite element computation of rate-dependent frictional sliding in large deformations, Comput. Methods Appl. Mech. Eng. 143 (1997) 197–227.
[8] D.K. Karupannasamy, J. Hol, M.B. de Rooij, T. Meinders, D.J. Schipper, Modelling mixed lubrication for deep drawing processes, Wear 294–295 (2012) 296–304.
[9] M. Ramezani, Z. Mohd Ripin, R. Ahmad, Modelling of kinetic friction in V-bending of ultra-high-strength steel sheets, Int. J. Adv. Manuf. Technol. 46 (2010) 101–110.
[10] E.R.M. Gelinck, D.J. Schipper, Calculation of Stribeck curves for line contacts, Tribol. Int. 33 (2000) 175–181.
[11] J.A. Greenwood, J.B.P. Williamson, Contact of nominally flat surfaces, Proc. R. Soc. London Ser. A 295 (1966) 300–319.
[12] H. Moes, Optimum similarity analysis with applications to elastohydrodynamic lubrication, Wear 159 (1992) 57–66.
[13] H. Moes, Lubrication and beyond, Lecture Notes Nr 115531, University of Twente, Enschede, The Netherlands, 2000.
[14] T.A. Laursen, Comput. Contact Impact Mech., Springer Verlag, Berlin, 2002.
[15] K.L. Johnson, J.A. Greenwood, S.Y. Poon, A simple theory of asperity contact in elastohydrodynamic lubrication, Wear 19 (1972) 91–108.
[16] T.E. Tallian, The theory of partial elastohydrodynamic contacts, Wear 21 (1972) 49–101.
[17] J. Rojek, E. Oñate, E. Postek, Application of explicit FE codes to simulation of sheet and bulk metal forming processes, J. Mat. Proc. Tech. 80–8l (1998) 620–627.

[18] J. Rojek, O.C. Zienkiewicz, E. Oñate, E. Postek, Advances in FE explicit formulation for simulation of metalforming processes, J. Mat. Proc. Tech. 119 (2001) 41–47.
[19] L. Taylor, J. Cao, A.P. Karafillis, M.C. Boyce, Numerical simulations of sheet-metal forming, J. Mat. Process. Technol. 50 (1995) 168–179.
[20] T.A. Laursen, The convected description in large deformation frictional contact problems, Int. J. Solids Struct. 31 (1994) 669–681.
[21] A. Konyukhov, K. Schweizerhof, Computational Contact Mechanics: Geometrically Exact Theory for Arbitrary Shaped Bodies, Springer, Heidelberg, 2013.
[22] A. Curnier, A theory of friction, Int. J. Solids Struct. 20 (1984) 637–647.
[23] J.E. Marsden, T.J.R. Hughes, Mathematical Foundations of Elasticity, Prentice-Hall, Inc., Englewood Cliffs, New Jersey, 1983.
[24] M. Scaraggi, G. Carbone, B.N.J. Persson, D. Dini, Mixed lubrication in soft contacts: a novel homogenized approach, Part I: Theory, Soft Matter 7 (2011) 10395–10416.
[25] B.N.J. Persson, M. Scaraggi, Lubricated sliding dynamics: flow factors and Stribeck curve, Eur. Phys. J. E Soft Matter 34 (2011) 113–135.
[26] X. Lu, M.M. Khonsari, E.R.M. Gelinck, The Stribeck curve: experimental results and theoretical prediction, ASME J. Tribol. 128 (2006) 789–794.
[27] T.-S. Yang, A refined friction modeling for lubricated metal forming process, Tribol. Lett. 27 (2007) 289–300.
[28] B.N.J. Persson, M. Scaraggi, On the transition from boundary lubrication to hydrodynamic lubrication in soft contacts, J. Phys.: Condens. Matter 21 (2009). 185002 (pp. 22).
[29] K.L. Johnson, Contact Mechanics, Cambridge University Press, Cambridge, 1985.
[30] B.N.J. Persson, Theory of rubber friction and contact mechanics, J. Chem. Phys. 115 (2001) 3840–3861.
[31] B.N.J. Persson, Contact mechanics for randomly rough surfaces, Surf. Sci. Rep. 61 (2006) 201–227.
[32] B. Lorenz, Contact mechanics and friction of elastic solids on hard and rough substrates, Schriften des Forschungszentrums Jülich 37 (2012).
[33] J.T. Oden, E. Pires, Nonlocal and nonlinear friction laws and variational principles for contact problems in elasticity, J. Appl. Mech. 50 (1983) 67–82.
[34] P. Wriggers, Computational Contact Mechanics, John Wiley & Sons, Chichester, 2002.
[35] P. Wriggers, G. Zavarise, Application of augmented lagrangian techniques for non-linear constitutive laws in contact interfaces, Commun. Numer. Methods Eng. 9 (1993) 815–824.
[36] Y. Hori, Hydrodynamic Lubrication, Springer, Tokyo, 2006.
[37] J. Durany, G. García, C. Vázquez, Numerical computation of free boundary problems in elastohydrodynamic lubrication, Appl. Math. Model. 20 (1996) 104–113.
[38] C.H. Venner, A.A. Lubrecht, Multi-level methods in lubrication, Tribology and Interface Engineering, Elsevier Science, vol. 37, Elsevier, 2000.
[39] B. Yang, T. Laursen, A mortar-finite contact approach to lubricated contact problems, Comput. Methods Appl. Mech. Eng. 198 (2009) 3656–3669.
[40] M. Selmani, L. Selmani, A frictional contact problem with normal damped response for elasto-visco-plastic materials, Rendiconti del Circolo Matematico di Palermo 59 (2010) 67–85.
[41] O. Chau, W. Han, M. Sofonea, A dynamic frictional contact problem with normal damped response, Acta Appl. Math. 71 (2002) 159–178.
[42] M. Luege, B.M. Luccioni, Numerical simulation of the lubricant performance in tube hydroforming, J. Mat. Process. Technol. 198 (2008) 372–380.
[43] J.H. Dieterich, Modeling rock friction: 1. Experimental results and constitutive equations, J. Geophys. Res. 84 (1979) 2161–2168.
[44] 0A.L. Ruina, Friction laws and instabilities: a quasistatic analysis of some dry frictional behavior, Ph.D.Thesis, Brown University, 1980.
[45] J.R. Rice, A.L. Ruina, Stability of steady frictional slipping, J. Appl. Mech. 50 (1983) 343–349.
[46] E.A. de Souza Neto, D. Peric, D.R.J. Owen, Computational Methods for Plasticity: Theory and Applications, Wiley, Chichester, 2008.
[47] T. Baumberger, L. Gauthier, Creeplike relaxation at the interface between rough solids under shear, J. Phys. 6 (1996) 1021–1030.
[48] J.M. Carlson, A.A. Batista, Constitutive relation for the friction between lubricated surfaces, Phys. Rev. E 53 (1996) 4153–4165.
[49] F. Heslot, T. Baumberger, B. Perrin, B. Caroli, C. Caroli, Creep, stick-slip, and dry-friction dynamics: experiments and a heuristic model, Phys. Rev. E 49 (1994) 4973–4987.
[50] Z. Yang, H.P. Zhang, M. Marder, Dynamics of static friction between stell and silicon, Proc. Natl. Acad. Sci. USA 105 (2008) 13264–13268.
[51] T. Baumberger, F. Heslot, B. Perrin, Crossover from creep to inertial motion in friction dynamics, Nature 367 (1994) 544–546.
[52] E. Rabinowicz, Friction and Wear of Materials, John Wiley and Sons, New York, 1965.
[53] A.L. Ruina, Slip instability and state variable friction laws, J. Geophys. Res. 88 (1983) 359–370.
[54] J.R. Rice, N. Lapusta, K. Ranjith, Rate and state dependent friction and the stability of sliding between elastically deformable solids, J. Mech. Phys. Solids. 49 (2001) 1965. 1898.
[55] C. Daly, J. Zhang, J.B. Sokoloff, Friction in the zero sliding velocity limit, Phys. Rev. E 68 (2003) 066118.
[56] M.H. Müser, How static is static friction?, Proc Natl. Acad. Sci. USA 105 (2008) 13187–13188.
[57] STAMPACK, Simulation software for multi-stage metal forming operations, Quantech, Barcelona, Spain.
[58] F-Y. Wang, L-P Wang, J-G Cheng, Z-H Tao, Contact force algorithm in explicit transient analysis using finite-element method, Finite Elem. Anal. Des. 43 (2007) 580–587.
[59] J.C. Simo, R.L. Taylor, Consistent tangent operators for rate-independent elastoplasticity, Comput. Methods Appl. Mech. Eng. 48 (1985) 101–118.
[60] A.E. Giannokopoulos, The return mapping method for the integration of friction constitutive relations, Comput. Struct. 32 (1989) 157–167.
[61] K.A. Grosch, The relation between the friction and visco-elastic properties of rubber, Proc. R. Soc. London Ser. A, Math. Phys. Sci. 274 (1963) 21–39.
[62] M. Barquins, A.D. Roberts, Rubber friction variation with rate and temperature: some new observations, J. Phys. D: Appl. Phys. 19 (1986) 547–563.
[63] R.J. Pinnington, Rubber friction on rough and smooth surfaces, Wear 267 (2009) 1653–1664.
[64] G. Luengo, F.-J. Schmitt, R. Hill, J. Israelachvili, Thin film rheology and tribology of confined polymer melts: contrasts with bulk properties, Macromolecules 30 (1997) 2482–2494.
[65] L.H. Lang, Z.R. Wang, D.C. Kang, S.J. Yuang, S.H. Zhang, J. Danckert, K.B. Nielsen, Hydroforming highlights: sheet hydroforming and tube hydroforming, J. Mat. Process. Technol. 151 (2004) 165–177.
[66] M. Ahmetoglu, J. Hua, S. Kulukuru, T. Altan, Hydroforming of sheet metal using a viscous pressure medium, J. Mat. Process. Technol. 146 (2004) 97–107.
[67] M. Luege, Numerical simulation of forming processes with hydroforming, Ph.D. Dissertation (in Spanish), National University of Tucumán, Argentina, 2006.